ASTRONOMICAL INSTITUTE
SLOVAK ACADEMY OF SCIENCES

CONTRIBUTIONS OF THE ASTRONOMICAL OBSERVATORY SKALNATÉ PLESO

• VOLUME LII •

Number 2

September 2022

ISSN: 1336–0337 (on-line version)

CODEN: CAOPF8

Editorial Office: Astronomical Institute of the Slovak Academy of Sciences
SK - 059 60 Tatranská Lomnica, The Slovak Republic

CONTENTS

STARS

SOLAR SYSTEM

The Contributions of the Astronomical Observatory Skalnaté Pleso
are available in a full version
in the frame of ADS Abstract Service
and can be downloaded in a usual way from the URL address:

https://ui.adsabs.harvard.edu/

as well as from the web-site of
the Astronomical Institute of the Slovak Academy of Sciences
on the URL address:

https://www.astro.sk/caosp/caosp.php

The journal is covered/indexed by:

Thomson Reuters services (ISI)
Science Citation Index Expanded (also known as SciSearch®)
Journal Citation Reports/Science Edition

SCOPUS

Contrib. Astron. Obs. Skalnaté Pleso **52/2**, 5 – 24, (2022)
https://doi.org/10.31577/caosp.2022.52.2.5

Detection of a cyclic period change in the contact binary TU UMi

D. Zengin Çamurdan[1] **and B. Özkardeş**[2,3]

[1] *Ege University, Science Faculty, Department of Astronomy and Space Sciences, 35100 Bornova,Izmir, Turkey, (E-mail: dicle.zengincamurdan@ege.edu.tr)*

[2] *Department of Space Science and Technologies, Faculty of Arts and Sciences, Çanakkale Onsekiz Mart University, Terzioğlu Kampüsü, TR-17020, Çanakkale, Turkey,*

[3] *Çanakkale Onsekiz Mart University, Astrophysics Research Center and Ulupınar Observatory, TR-17100, Çanakkale, Turkey*

Received: February 7, 2022; Accepted: April 26, 2022

Abstract. This study aims at timing the eclipses of the binary star TU UMi. The times of minima are taken from the literature, from our observations in April 2004 and from TESS observations between 2019 and 2022. The orbital period analysis of the system indicates that there is a cyclic oscillation with an amplitude of 0.0081d and a period of 9.03 yr, accompanied by a continuous decrease at a rate of $dP/dt = -1.12 \times 10^{-7}\,\mathrm{d\,yr^{-1}}$. We study the secular evolution of the orbital period of the system and the possibility of the existence of a third companion or the magnetic activity cycle of the primary component in the system.

Key words: Stars: binaries: eclipsing; Stars: Individual TU UMi

1. Introduction

Variability of TU UMi (BD+76544, HIP 73047) was detected during the Hipparcos mission (ESA, 1997) with a period of $0^d.188546$. Duerbeck (1997) reported the system as a contact binary of EW, or a pulsating star with a doubled period. Kazarovets et al. (1999) and Rodríguez et al. (2000) classified the source as a delta Scuti type variable star. However, Rolland et al. (2002) observed the system in Strömgren filters and showed that TU UMi is outside of the instability strip of delta Sct-type pulsators using a colour-magnitude diagram.

TU UMi was observed spectroscopically by Pych & Rucinski (2004) who reported that TU UMi is a triple system containing a close binary and the light contribution of the third component around the contact binary is $L_3/(L_1+L_2) = 1.25 \pm 0.15$. Pych & Rucinski (2004) also determined the period of TU UMi at twice the Hipparcos original period. Rucinski et al. (2005) presented the first radial velocity orbit of the system: $K_1 = 35 \pm 15\ kms^{-1}$, $K_2 = 220 \pm 20$

kms^{-1} and the radial velocity of for the third companion is -4.16 ± 0.20 kms^{-1}. They calculated the mass function of $(M_1 + M_2)sin^3i = 0.65 \pm 0.27 M_\odot$ and an extremely low mass ratio of $M_2/M_1 = 0.16\pm0.07$ and classified it as an EW/W-type binary. Kjurkchieva et al. (2010) observed brightness changes of the system in BVR filters. They reported that the light curves of the system are asymmetric with steeper decreasing branches and unequal maxima and suggested that the third bright companion may be responsible for these variations. Furthermore, TU UMi was included in the Asteroseismic Target List (Schofield et al., 2019) of solar-like oscillators to be observed in 2-minute cadence with TESS and some of the fundamental parameters combining the Gaia DR2 and Hipparcos data were given in this study. Although the minima times of the system were reported by many researchers, the O-C period variation was only pointed out by Kjurkchieva et al. (2010), who analyzed the data from the years 2003-2009. Based on a 6-year eclipsing cycle of TU UMi, Kjurkchieva et al. (2010) interpreted that the O-C values are increasing linearly in time as the consequence of the low precision of the determined period.

In this paper, we reconsidered all reported minima times in the literature and used the TESS data which were obtained between 2019 and 2022, and the $UBVR$ observations that were obtained in 2004 at the Ege University Observatory, as well. The period change was then investigated in detail, based on all available light minimum times and the results are presented. Here, we report on the detection of a long-term period decrease superimposed on a cyclic change in the orbital period of TU UMi and discuss the plausible cause of these period changes. We performed the solution of the light-travel time effect (LITE) via the presence of an additional companion and magnetic activity cycle for TU UMi with new minima times.

2. Observations and determinations of the times of minima

Johnson $UBVR$ observations of TU UMi in terms of differential magnitudes with respect to the comparison star HD131358 were carried out at the Ege University Observatory (EUO) with the 0.48-m Cassegrain telescope equipped with a high-speed three-channel photon-counting photometer (Kalytis, 1999). Fainter comparison and check stars (i.e. Comp. and Chk.) were chosen and are listed in Tab. 1. The observations were performed during 8 nights in 2004 in $UBVR$ bands and typical exposure times were 10 s. We obtained a total of 432 measurements in all bands. All differential magnitudes were corrected for atmospheric extinction and heliocentric corrections were applied to all observing times. The amplitudes of variable light are 0.055^m, 0.056^m, 0.062^m, and 0.052^m for $UBVR$ bands, respectively. Hence, both eclipse depths are shallow and it is difficult to distinguish primary and secondary minima in our observations. The primary eclipse is deeper than the secondary one by up to 0.005^m. Since our

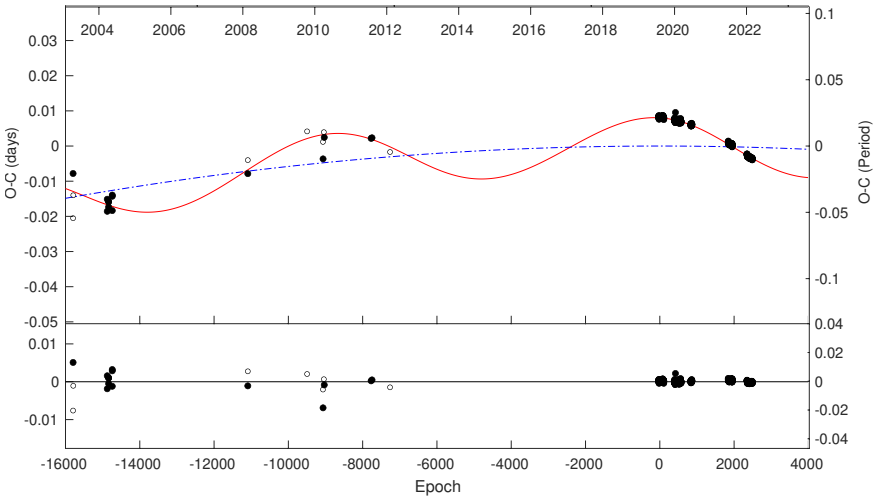

Figure 1. The *O-C* diagram of TU UMi (upper part), where the solid line represents the theoretical LITE variation caused by a 3rd body and the dashed line represents the quadratic ephemeris, and the *O-C* residuals obtained after the subtraction of LITE (lower part).

major goal is to obtain differential photometry for program stars, we did not observe photometric standard stars during our runs.

Tab. 1 gives an observing log for data observed at the Ege University Observatory (EUO). To study orbital period changes, we collected a total of 14 light minimum times. From the new observations, eight light minimum timings were determined by the least-squares fit of the observed data using the K-W method (Kwee & van Woerden, 1956). Furthermore, The TESS light curves of TU UMi are used to determine the mid-times of primary and secondary eclipses of the system, where we obtain 904 minima times in total, of which 454 are the primary minima and 450 the secondary times of minimum. The minima times data come from observations sector 14, 15, 20, 21, 22, 26, 40, 41, 47, and 48. Forty-five computed minima times using TESS data are included in Tab. 2, while the rest of them are available upon request. Those individual light minimum times, together with their errors, and the *O-C* residuals are listed in Tab. 2.

Table 1. Coordinates of the variable, comparison and check stars.

Star	$\alpha_{J2000.0}$	$\delta_{J2000.0}$	mag (V)
TU UMi	14 55 43.80	+76 18 23.65	8.75 ± 0.01
HD 131358 (Comp.)	14 47 10.16	+76 02 32.13	7.38 ± 0.01
HD 135118 (Chk.)	15 06 53.63	+75 59 07.04	8.29 ± 0.01

3. Analysis of period change

The eclipse timing data used in the *O-C* analysis of TU UMi covers almost 19 years from March 2003 to February 2022. An *O-C* diagram with all those timings is plotted in Fig. 1 by using the following light element, where T_0 = 2458696.10801 (HJD) and $P = 0^d.377088$ are the conjunction time obtained in this study from TESS observations and the orbital period taken from Rucinski et al. (2005), respectively.

The *O-C* diagram including minimum times using the TESS data is shown in Fig. 1. As it can be seen in the figure, a systematic deviation from the linear ephemeris is present in the current *O-C* diagram and it has a downward curving parabolic character indicating a period decrease of the system, which was not discovered by the previous *O-C* diagrams (Kjurkchieva et al., 2010). However, with the current data, one additional structure in the *O-C* diagram came out which can be seen in the residuals from the parabolic approximation in Fig. 1. This additional structure has a cyclic character superimposed on the general quadratic trend. We have quickly tested the significance of this cyclic character by looking at the difference in the values of the sum of squared residuals of the fits to the *O-C* data with only parabolic and parabolic+cyclic approximations. The sum of squared residuals $\Sigma(O-C)^2$ turns out to be 0.021 day^2 and 0.0026 day^2 for only parabolic and parabolic+cyclic fits, respectively. As seen from these values the sum of squared residuals substantially improved when the cyclic variation has been taken into account.

To search for the period of the cyclic variations, a periodogram analysis with PERIOD04 (Lenz & Breger, 2005) was carried out for the quasi-sinusoidal variation seen in the residuals of *O-C* after the subtraction of a quadratic term, whose result is displayed in Figure 2. We found a significant peak in the power spectrum mainly located around the frequency of $f_1 = 3.00744 \times 10^{-4}\,\mathrm{d}^{-1}$, which corresponds to a period of 3325 days ($\sim$ 9.1 yr). This value is then used as an initial P_{mod} parameter for the non-linear least-squares fitting the *O-C* values.

The cyclic variations are usually explained either by the light travel time effect (LTTE) via the presence of a third body, or by magnetic activity cycles in one or both components because they are late-type stars. To search for the LTTE effect, the calculated the *O-C* values based on all times of minima were fitted by the equation:

$$\begin{aligned} O-C =& O-[T_0 + P_{orb}\times E + \frac{1}{2}\frac{dP}{dE}\times E^2 + \\ & \frac{A}{\sqrt{1-e^2\,cos^2\,\omega}}\times\left\{(1-e^2)\frac{sin\,(\nu+\omega)}{(1+e\,cos\,\nu)}\right\} \end{aligned} \tag{1}$$

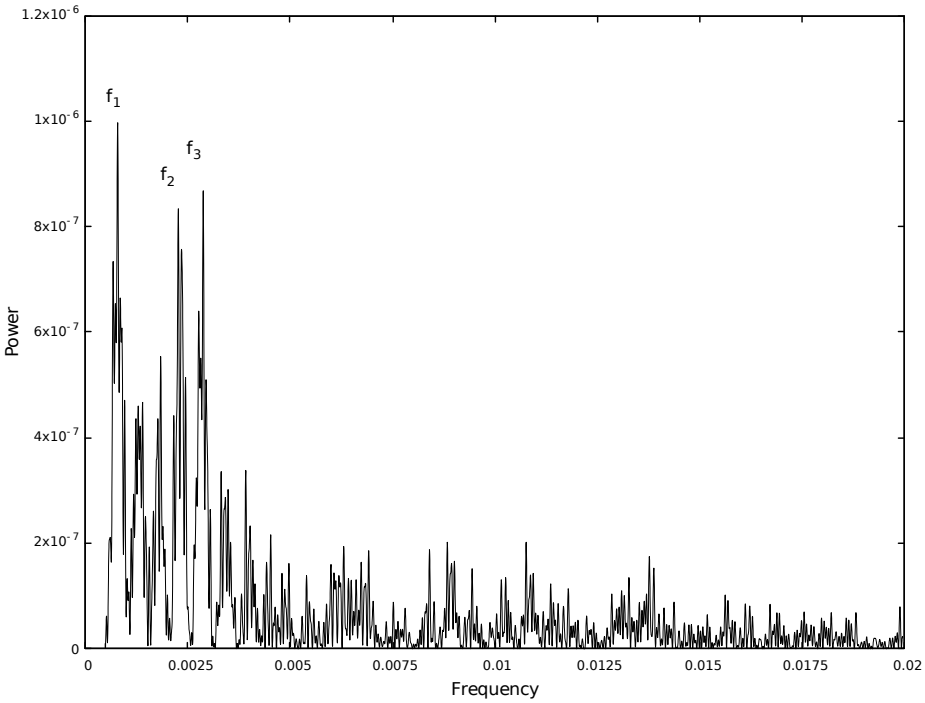

Figure 2. The power spectrum of the residuals from the quadratic fit.

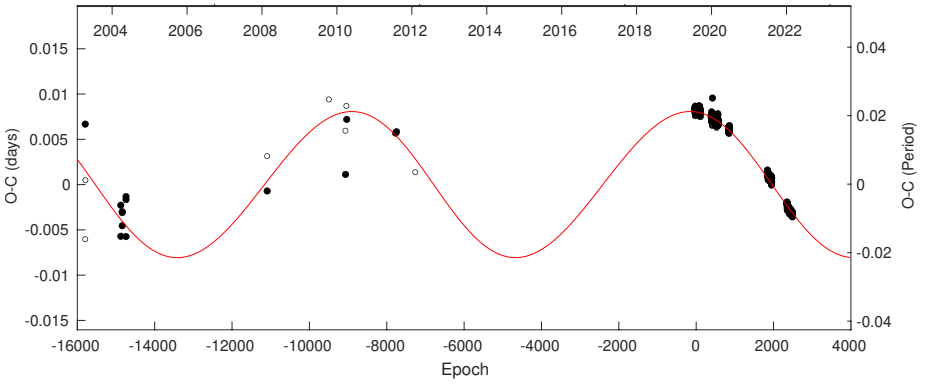

Figure 3. The *O-C* curve of TU UMi shows the residuals from the quadratic fit. The solid line refers to a theoretical orbit of the additional component in the system.

where

$$A = \frac{a_{12}\, sin\, i\sqrt{1 - e^2\, cos^2\, \omega}}{2.590 \times 10^{10}}$$

is the semi-amplitude of the light-time effect in days. E, P_{orb}, T_0 and dP/dE represent the cycle number, orbital period, the reference epoch for the primary minimum and the rate of the secular period change of the binary star, respectively. a_{12}, i, e and ω, 2.590×10^{10} are the semi-major axis, inclination, eccentricity, longitude of the periastron of the absolute orbit of the center of mass of the eclipsing binary around the three-body system and the speed of light in km/day, respectively. ν is the true anomaly of the position of the eclipsing binarys mass center on this orbit and includes T_p that it is the epoch of the passage at the periastron of the eclipsing binarys mass center along its orbit and P_{mod}, which is the modulation period of the third body orbit.

The *O-C* method was applied in the analysis using a matlab code given by Zasche et al. (2009) to determine the eight free parameters (namely T_0, P_{orb}, dP/dE, P_{mod}, T_p , $a_{12}\, sini$, e, ω) by least-squares fitting the *O-C* values taking into account both variations (parabolic+cyclic). The best theoretical fit made to the $O-C$ diagram and the residuals obtained from the fit are shown in Fig. 1 and Fig.3 and the derived parameters and their errors are given in Tab. 3. The sum of square residuals from the best fit is 0.0026 days^2.

4. Results and conclusions

4.1. Mass transfer between the components

TU UMi is a short-period ($0^{\rm d}.3770$) W-type contact binary where the primary component is estimated to be F-type star by Rucinski et al. (2005) and is poorly investigated in detail. By analyzing a total of 926 times of light minimum, the orbital period of TU UMi is changing with a cyclic character superimposed on a decreasing structure. The *O-C* curve of the system shows a clear long-term period decrease at a rate of $dP/dt = -1.12 \times 10^{-7}\,{\rm d\,yr^{-1}}$ ($-0.18\,{\rm sec\,century^{-1}}$). The type of variations, i.e., a long-term decrease combined with a cyclic change, is commonly found in W UMa-type stars that are shown in Tab. 4 for some of the W-type contact binaries between $0.2\,{\rm d} < P_{orb} < 0.7\,{\rm d}$. Furthermore, Li et al. (2018) studied the light travel-time effect in short-period eclipsing binaries and concluded that the frequency of third bodies found in contact binaries with $P < 0.3$ day reaches a value of 0.65 in their samples including 542 eclipsing binaries. Therefore, there may exist a periodic variation superimposed on a secular decrease in the period in the *(O-C)* curve of TU UMi. The long-term period decrease can be explained by mass transfer from the more-massive component to the less-massive one in the case of a conservative mass transfer, or by the angular momentum loss from the system, or by a combination of both mechanisms.

Table 2. Observed times and *(O-C)*[d] values of minimum light for TU UMi.

BJD[1]2400000+)	Error	Epoch	$(O-C)_1$	$(O-C)_2$	Residuals	Reference
52739.5938	0.0004	-15796.0	-0.0071	0.0067	0.0051	[1]
52739.7696	0.0008	-15795.5	-0.0198	-0.0061	-0.0076	[1]
52741.6616	0.0003	-15790.5	-0.0133	0.0005	-0.0011	[1]
53086.5050	0.0020	-14876.0	-0.0179	-0.0057	-0.0019	[2]
53086.5084	0.0022	-14876.0	-0.0145	-0.0023	0.0016	[2]
53100.4599	0.0043	-14839.0	-0.0153	-0.0031	0.0010	[2]
53100.4577	0.0023	-14839.0	-0.0167	-0.0046	-0.0005	[2]
53100.4600	0.0011	-14839.0	-0.0152	-0.0030	0.0011	[2]
53137.4122	0.0009	-14741.0	-0.0178	-0.0058	-0.0012	[2]
53137.4163	0.0010	-14741.0	-0.0137	-0.0017	0.0029	[2]
53137.4166	0.0008	-14741.0	-0.0134	-0.0014	0.0032	[2]
54513.4207	0.0006	-11092.0	-0.0075	-0.0007	-0.0011	[3]
54513.6131	0.0008	-11091.5	-0.0037	0.0031	0.0028	[3]
55115.4555	–	-9495.5	0.0049	0.0099	0.0020	[4]
55276.4695	0.0009	-9068.5	0.0019	0.0064	-0.0021	[5]
55277.4074	0.0010	-9066.0	-0.0030	0.0016	-0.0069	[5]
55285.5224	0.0009	-9044.5	0.0046	0.0092	0.0007	[5]
55289.4804	0.0012	-9034.0	0.0031	0.0077	-0.0008	[5]
55765.3665	0.0003	-7772.0	0.0025	0.0059	0.0002	[6]
55774.4168	0.0002	-7748.0	0.0027	0.0060	0.0005	[6]
55957.4895	0.0010	-7262.5	-0.0014	0.0015	-0.0015	[7]
58690.8294	0.0001	-14.0	0.0086	0.0086	0.0001	[2]
58690.6406	0.0001	-14.5	0.0083	0.0083	-0.0002	[2]
58731.3663	0.0001	93.5	0.0084	0.0084	0.0000	[2]
58731.5551	0.0001	94.0	0.0086	0.0086	0.0002	[2]
58853.5425	0.0001	417.5	0.0077	0.0077	0.0000	[2]
58853.7313	0.0001	418.0	0.0079	0.0079	0.0002	[2]
58883.3323	0.0001	496.5	0.0075	0.0075	-0.0001	[2]
58883.5211	0.0001	497.0	0.0076	0.0076	0.0001	[2]
58908.4085	0.0001	563.0	0.0072	0.0072	-0.0001	[2]
58908.5971	0.0001	563.5	0.0072	0.0072	-0.0001	[2]
59021.3459	0.0001	862.5	0.0064	0.0065	0.0002	[2]
59021.5346	0.0001	863.0	0.0065	0.0066	0.0003	[2]
59403.1432	0.0001	1875.0	0.0010	0.0012	0.0004	[2]
59403.3318	0.0001	1875.5	0.0011	0.0013	0.0004	[2]
59431.0473	0.0001	1949.0	0.0005	0.0007	0.0003	[2]
59431.2359	0.0001	1949.5	0.0006	0.0008	0.0004	[2]
59580.7490	0.0001	2346.0	-0.0033	0.0000	0.0002	[2]
59580.9372	0.0001	2346.5	-0.0036	-0.0003	-0.0002	[2]
59606.3901	0.0001	2414.0	-0.0030	-0.0027	-0.0003	[2]
59606.5787	0.0001	2414.5	-0.0029	-0.0026	-0.0002	[2]
59610.5381	0.0001	2425.0	-0.0030	-0.0027	-0.0003	[2]
59610.7267	0.0001	2425.5	-0.0029	-0.0026	-0.0002	[2]
59635.4258	0.0001	2491.0	-0.0032	-0.0029	-0.0001	[2]
59635.6142	0.0001	2491.5	-0.0033	-0.0029	-0.0001	[2]

[1] The minimum times are in the barycentric dynamical time system (BJD).

Notes: [1] Pych & Rucinski (2004); [2] Present work; [3] Brát et al. (2008); [4] Kjurkchieva et al. (2010); [5] Liakos & Niarchos (2010); [6] Soydugan et al. (2017); [7] Hubscher (2013).

Table 3. Parameters derived from (O-C) analysis.

Parameter	Value	Error
Parabolic behavior related		
T_0 [BJD]	2458696.1005	0.0001
P_{orb} [days]	0.37708906	0.00000008
dP/dt [days/year]	-1.12×10^{-7}	0.01×10^{-7}
3^{rd} body related		
$a_{12}\, sin\, i$ [AU]	1.398	0.009
e	0.05	0.01
ω [degree]	0.3	24.6
T_p [BJD]	2462732.2	213.7
P_{mod} [year]	9.03	0.02
A [days]	0.0081	0.0001
$f(M_3)$ [$M_\odot$]	0.03352	0.00001
$M_3(i = 90°)$ [$M_\odot$]	0.61145	0.00007
$M_3(i = 60°)$ [$M_\odot$]	0.72665	0.00009
$M_3(i = 30°)$ [$M_\odot$]	1.48124	0.00022
Magnetic activity cycle related		
ΔJ [gcm^{2}s^{-1}]	7.66×10^{47}	
$\Delta\Omega/\Omega$	3.08×10^{-3}	
B[kG]	22.9	

The period investigation of Kjurkchieva et al. (2010) showed that the O-C variation of TU UMi was linear. However, only times of light minima observed between 2003 and 2009 were used in their work. In our O-C diagram, times of light minima obtained by the high accuracy TESS data are used and these data show a downward tendency. Therefore, the TESS data are very important when the period variation of TU UMi is investigated since they will give a quite different result, as shown in Fig. 1 and Fig. 3. Also, a cyclic period change is revealed for the first time in this study. Assuming that the long-term period change of the system can be explained by mass transfer, then some parameters, including the masses of the two components ($M_1 = 1.313\, M_\odot, M_2 = 0.21\, M_\odot$)[1], period, the rate of change of the period of TU UMi were used in the following equation to calculate the rate of mass transfer:

$$\dot{M} = \frac{M_1.M_2}{3(M_1 - M_2)} \frac{\dot{P}}{P}; \tag{2}$$

thus, $dM/dt = 0.25 \times 10^{-7} M_\odot yr^{-1}$ was determined, assuming that the more massive star transfers its present mass to the less massive component on a thermal timescale τ_{th} (Paczyński, 1971) , $\tau_{th} = 1.2 \times 10^7$yr and mass is transferred to the companion at a rate of $M_1/\tau_{th} = 1.1 \times 10^{-7} M_\odot yr^{-1}$. This value is compatible with the calculated one using the observed period change. This means that mass transfer can describe the parabolic variation.

[1]We should state that the absolute values of masses of the system used in this section are taken from Zhang & Qian (2020) calculated by using equations given in Gazeas (2009) (equations 710) where the mass ratio ($q = m_2/m_1$) is about 0.16 (from spectroscopic observation given by Rucinski et al. (2005)).

Table 4. Some of the W-type contact binaries with a period decrease.

Name	P_{orb} (days)	q	M_1 $M_\odot$	M_2 $M_\odot$	dP/dt ($\times 10^{-7}$dyr^{-1})	dM/dt ($\times 10^{-7}M_\odot$yr^{-1})	Cylic	P_{cyc} (years)	LTTE	Ref.
CC Com	0.2207	0.52	0.79	0.41	-0.40	0.51	yes	16.1	yes	[1]
V1104 Her	0.2279	0.63	0.74	0.46	-0.29	0.52	yes	8.28	yes	[2,3]
YZ Phe	0.2347	0.38	0.74	0.28	-0.26	0.17	yes	40.76	yes	[4]
RW Com	0.2370	0.48	0.80	0.38	-0.43	0.44	yes	13.70	yes	[5,6]
EI CVn	0.2608	0.46	0.63	0.29	-3.11	1.03	unclear	4.96	-	[7]
V1197 Her	0.2627	0.38	0.77	0.30	-2.58	1.61	unclear	-	-	[8]
EH CVn	0.2636	0.30	0.67	0.20	-0.52	0.19	unclear	-	-	[9]
GV Leo	0.2667	0.19	1.09	0.19	-4.95	1.42	unclear	-	-	[10]
BM UMa	0.2712	0.54	0.92	0.50	-0.75	1.01	yes	30.8	unclear	[11]
VW Cep	0.2787	0.30	1.13	0.34	-1.69	0.98	yes	7.62	yes	[12]
V1005 Her	0.2789	0.30	0.92	0.98	-1.59	0.76	yes	18.1	yes	[13]
BX Peg	0.2804	0.37	1.02	0.38	-0.98	0.71	yes	16	unclear	[14]
V524 Mon	0.2836	0.48	0.99		-0.002	0.002	yes	23.9	unclear	[15]
RW Dor	0.2854	0.63	0.97	0.61	-0.14	0.27	unclear	49.9	-	[16]
LO Com	0.2864	0.40	0.79	0.32	-1.18	0.74	unclear	-	-	[17]
V842 Cep	0.2889	0.44	0.76	0.33	-1.50	1.01	unclear	-	-	[18]
EP Cep	0.2897	0.15	0.73	0.11	-3.73	0.56	unclear	-	-	[19]
TZ Boo	0.2974	0.21	0.72	0.11	-0.21	0.03	yes	31.2	unclear	[20]
V2284 Cyg	0.3069	0.35	0.86	0.30	-2.67	1.34	yes	2.06	yes	[21]
TY Boo	0.3171	0.47	1.21	0.57	-3.6	0.41	yes	58.9	yes	[22]
FG Hya	0.3278	0.11	1.44	0.16	-1.96	0.36	yes	36.4	unclear	[23]
V781 Tau	0.3449	0.45	1.06	0.43	-0.32	0.22	yes	30.8	unclear	[24]
V417 Aql	0.3700	0.37	1.40	0.50	-0.55	0.39	yes	42.4	unclear	[25]
AP Leo	0.3703	0.30	1.47	0.44	-1.08	0.61	yes	22.4	unclear	[26]

Table 4. Continued.

Name	P_{orb} (days)	q	M_1 $M_\odot$	M_2 $M_\odot$	dP/dt ($\times 10^{-7}$dyr^{-1})	dM/dt ($\times 10^{-7}M_\odot$yr^{-1})	Cylic	P_{cyc} (years)	LTTE	Ref.
V396 Mon	0.3963	0.39	0.92	0.36	-0.86	0.51	yes	42.4	yes	[27]
SS Ari	0.4060	0.36	1.30	0.40	-1.56	0.74	yes	39.7	unclear	[28]
MR Com	0.4127	0.26	1.40	0.36	-5.30	2.07	yes	10.1	yes	[29]
BS Cas	0.4408	0.28	1.20		-1.51	0.54	yes	13.2	unclear	[30]
TV Mus	0.4457	0.17	1.35	0.22	-2.16	0.42	yes	29.1	unclear	[31]
V502 Oph	0.4534	0.34	1.42	0.48	-1.68	0.88	yes	23	yes	[32,33,34]
GU Ori	0.4706	0.43	1.05	0.45	-0.62	0.35	unclear	-	-	[35]
IK Per	0.6760	0.19	1.99	0.34	-2.52	0.51	yes	50.5	yes	[36]

Notes: [1] Yang & Liu (2003) ; [2] Liu et al. (2015); [3] Latković et al. (2021a);[4] Sarotsakulchai et al. (2019b) ;[5] Yang & Liu (2003) ;[6] Djurašević et al. (2011); [7] Yang (2011); [8] Zhou & Soonthornthum (2020) ; [9] Xia et al. (2018) ; [10] Kriwattanawong & Poojon (2013) ; [11] Yang et al. (2009) ; [12] Mitnyan et al. (2018) ; [13] Zhu et al. (2019) ;[14] Lee et al. (2009) ;[15] He et al. (2012) ;[16] Sarotsakulchai et al. (2019a) ;[17] Zhang et al. (2016) ;[18] Li et al. (2021) ;[19] Zhu et al. (2014) ;[20] Christopoulou et al. (2011) ;[21] Wang et al. (2017) ;[22] Christopoulou et al. (2012) ;[23] Qian & Yang (2005) ;[24] Lu et al. (2020) ;[25] Qian (2003);[26] Qian et al. (2007) ;[27] Liu et al. (2011);[28] Kim et al. (2003);[29] Qian et al. (2013);[30] Yang et al. (2008);[31] Qian et al. (2005) ;[32] Pych et al. (2004);[33] Maceroni et al. (1982);[34] Liu & Yang (2006) ;[35] Zhou et al. (2018) ;[36] Zhu et al. (2005) .

4.2. Cyclic variation

The *O-C* residuals obtained after the subtraction of the quadratic term are shown in Figure 3, whose shape appears to have a quasi-sinusoidal variation with a period of $\sim$ 9 yr. This can be explained in two ways: the Applegate mechanism (Applegate, 1992) and the light-time effect.

4.2.1. Presence of a possible third component

One of the possible causes of the cyclic *O-C* variation may be the light travel time effect (LTTE) due to a third body that is physically bound to the system. In order to examine this situation, the LTTE equation given by Irwin (1952) (see Equ. 1) was fitted to the *O-C* diagram of the system.

According to the parameters given in Tab. 3, TU UMi orbits around the triple systems center of mass in a very low eccentric orbit ($e = 0.05 \pm 0.01$) with a period of $P_{mod} = 9.03 \pm 0.02$ years. The projected distance of the center of mass of TU UMi to the center of mass of the three-body system was estimated to be $a_{12}\, sin\, i = 1.398 \pm 0.009$ AU. Using the P_{mod} and $a_{12}\, sin\, i$ values, the mass function of the third body was found to be $f(M_3) = 0.03352 \pm 0.000001\, M_\odot$. The minimum mass of the tertiary ($i = 90°$, where i is the inclination of the third bodys orbit) is estimated as $M_3 = 0.611\, M_\odot$. According to Budding & Demircan (2007)'s empirical main sequence table, the spectral type of this companion is estimated to be $\sim$ K3. Therefore, the third body deduced from LTTE may be a low-mass star. In this case, the mass of the third body is comparable to the mass of the secondary component in the binary system. Pych & Rucinski (2004) reported that TU UMi is a triple system containing a close binary and about 50 percent of total light coming from the bright tertiary companion in the system. However, this system is also known as a visual binary[2] with a separation of 0.2 arcsec. Rucinski et al. (2005) suggest that the third, spectroscopic component is probably identical to the visual component. Apart from this, the third body was not confirmed photometrically and further observational evidence for the existence of a third body needs to be investigated. If the third body is really present in the system, it may have an important role in the evolution of the binary system by drawing angular momentum from the central binary via a Kozai cycle (Kozai, 1962) or a combination of a Kozai cycle and tidal friction.

4.2.2. Magnetic activity

The close binary systems with late-type components are well known to be magnetically active, e.g. with chromospheric emission, starspots. The Applegate mechanism suggests that magnetic activity causes a variation of the angular momentum distribution, and then leads to variations in the active component

[2]The visual component is WDS 14557+7618.

in the system. So any change in the rotational system of a binary star component due to the magnetic activity will be reflected to the orbit as a consequence of the spin-orbit coupling and the orbital period changes slightly periodically.

The observed cyclic variation in the *O-C* diagram of TU UMi may be explained as resulting from magnetic activity variations due to star spots. We have calculated the activity related parameters by following the Applegate (1992) formulation and assuming the primary component (should be an F2 type dwarf according to the (*B-V*) color index value given by Duerbeck (1997)) of the system is responsible from the activity. The parameters are the cycle modulation, period $P_{cyc} = 9.03$ years, the amplitude of the cyclic period variation, $\Delta P = 1.005$ sec cycle^{-1}, the angular momentum transfer $\Delta J = 7.66 \times 10^{47}\,\mathrm{g\,cm^2\,s^{-1}}$ required to produce the observed cyclic effect on the orbital period, required energy $\Delta E = 2.28 \times 10^{41}$ ergs for the ΔJ transfer, the corresponding luminosity change $\Delta L = 0.633\,L_\odot$, and, finally the subsurface magnetic field $B = 22.9\,\mathrm{kG}$ of the primary component. The period variation $\Delta P/P$ can be used for calculating the variation of the quadruple moment ΔQ and this quantity results in $2.15 \times 10^{50}\,\mathrm{g\,cm^2}$, which is within the limits for active binaries (a range of values from 10^{50} to $10^{51}\,\mathrm{g\,cm^2}$). Since the parameters of the two components of the binary were adopted by Zhang & Qian (2020), we can calculate the changes of the luminosity to be $\Delta L_1 = 0.633\,L_\odot < L_1\,(3.2\,L_\odot)$. Obviously, the active primary component can provide enough energy to generate such changes. Therefore, the Applegate mechanism can explain the cyclic period change in TU UMi as well. In addition, we should point out that no unequal difference between the two light maxima (Max I-Max II), or the OConnell effect was not remarkable in the TESS and our observations. In addition to this, according to Tran et al. (2013), strong spot activity causes an effect on the variations of the minima times. The trends of primary and secondary minima time variations are expected to show an erratic, and anticorrelated to each other behaviour and these have been observed in many W UMa type systems. To search for such a variation in our case, we decided to plot primary and secondary *O-C* times determined from TESS data. As TU UMi was observed by TESS intermittently during the period March 2003 to February 2022, we focus on two consecutive data sets (Sector 21, 22 and Sector 47, 48). As it can be seen in Fig. 4, there are no short-term, anticorrelated *O-C* variations in the primary and secondary curves of TU UMi. The results may suggest that TU UMi has a very weak activity and it may be in an inactive state for decades with no significant spot activities. The Applegate mechanism also supports the long-term light variation and the *O-C* curve formed by the times of minima should have the same cycle length. Unfortunately, we do not have precise enough long-term photometric observations for TU UMi to check such brightness variations. Long-term photometric monitoring can clarify TU UMi's plausible magnetic activity cycle characteristics.

We calculated the angular momentum loss (AML) via magnetic stellar wind which can be determined by the following equation given by Bradstreet &

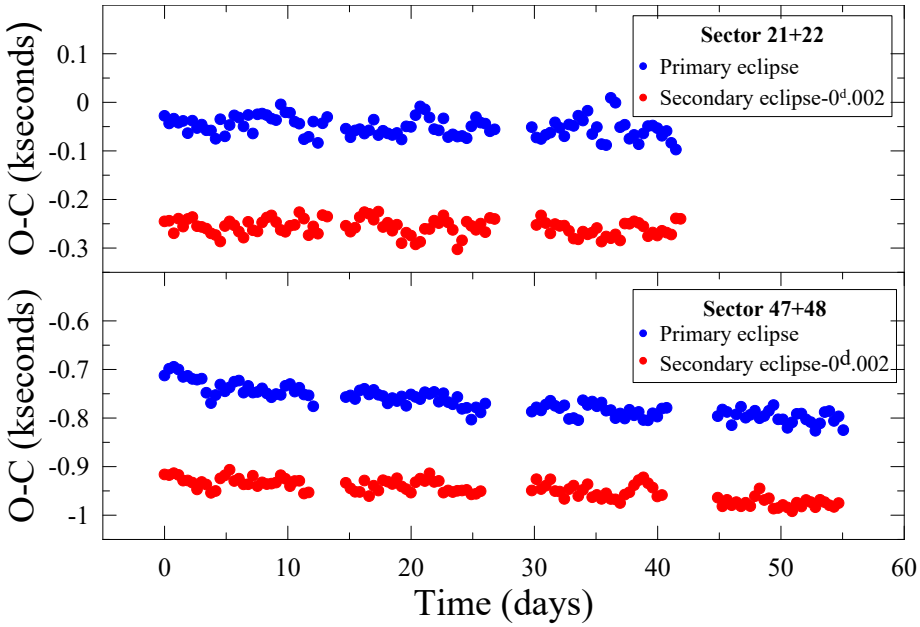

Figure 4. Time-dependent variations of the *O-C* curves for the primary and secondary eclipses (vertically displaced for clarity) are shown as blue and red colors for Sector 21, 22 (top panel), and Sector 47, 48 (bottom panel), respectively.

Guinan (1994) for the long-term decrease:

$$\dot{P} \approx 1.1 \times 10^{-8}\, q^{-1}\, (1 + q^2\, (M_1 + M_2)^{-5/3} \times k^2\, (M_1\, R_1^4 + M_2\, R_2^4)\, P^{-7/3} \tag{3}$$

where k^2 is the gyration constant between 0.07 to 0.15 for solar-type stars. By adopting the value of $k^2 = 0.1$, the rate of the orbital period decrease due to AML can be computed as $dP/dt \sim 2.4 \times 10^{-7}\,\mathrm{d\,yr^{-1}}$ and the timescale of the period decrease is $(dP/dt) \sim 1.56 \times 10^6\,\mathrm{yr}$ or ~ 1.6 Myr) which is close to the timescale from observed the period decrease derived from $O - C$ variation $(P/(dP/dt) = 2.6$ Myr). This may lead to the conclusion that the long-term period decrease of TU UMi can also be constrained by AML, but as it can be seen in Sec. 4.1, the period decrease from conservative mass transfer cannot be neglected. Therefore, a plausible explanation for the long-term period decrease in TU UMi is AML, or the combination of the two mechanisms (AML and mass transfer). Nevertheless, observations in the next decades are necessary to clarify the true shape of the *O-C* diagram.

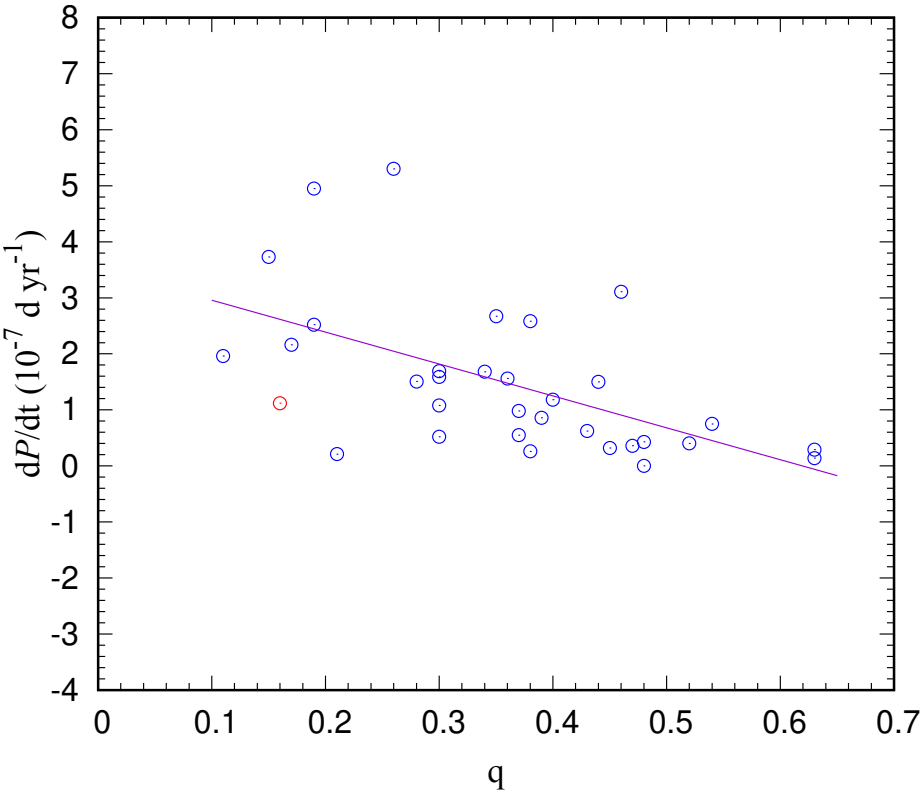

Figure 5. A plot of the period change range versus the mass ratio (dP/dt- q) for some W-type systems (blue circles) listed in Tab. 4. For comparison, the parameters of TU UMi (red circles) are also plotted. The fitted curve is given in Eq. 4.

4.2.3. Long-term period decrease in W-type W UMa stars

Long-term period decreasing and increasing are common for W UMa-type binaries. This variation is usually due to mass transfer or angular momentum loss, which results in orbital period changes. In this study, the analysis of the orbital period of TU UMi was performed and a long-term period decrease was discovered. In general, it is interpreted as caused by conservative mass transfer from the more massive component to the less massive component. In order to find a relation between the observed period change rate using $O-C$ variation and the mass ratios, we compiled the physical parameters and the observed period change rate (dP/dt) for some W-type contact binaries showing a secular period change plus cyclic variations in the literature in a period range of $0.2 < P_{orb} < 0.7$ d. They are listed in Tab. 4 in the order of the increasing orbital

period. The plot of the period change versus the mass ratio rate can be seen in Fig. 4, where the positions of 32 W-type W UMa stars are shown. Based on these parameters, there may exist a correlation (solid line) between the period change, dP/dt, and the mass ratio, q. We fitted the data using the least-squares method and the fitting result yields the following equation:

$$dP/dt = -5.82(\pm 1.55)\, q + 3.60(\pm 0.60), \tag{4}$$

where dP/dt is in units of $\times 10^{-7}$ d yr^{-1}. This relation tells us that the secular periods of systems are decreasing with the increasing mass ratio. It seems that the mass transfer between the two components may contribute to changes in the mass ratio of a system, which needs to be confirmed using a large sample of W UMa stars. However, in a statistical study for contact binaries by Latković et al. (2021b), there has been recently investigated the relation between the orbital period change rate (taking into account both period increasing and decreasing) and the mass ratio for A and W-type systems using a large sample of W UMa stars. They pointed out that there is no correlation between the type of period variability and the mass ratio (see their Fig. 7). In our sample, it seems that the derived relation is more obvious for $q > 0.25$. The systems with $q < 0.25$ tend to show dP/dt in a large range of $(2 - 5.3) \times 10^{-7}$ d yr^{-1}. The maximum dP/dt value is 3×10^{-7} d yr^{-1} for the systems with $q > 0.25$. The q value of TU UMi shows that it is in agreement with the observed period change rates of W-type W UMa binaries. Tab. 4 also lists the estimated mass transfer rates of samples, we found them to be in the range $(0.002 - 2) \times 10^{-7} M_{\odot} yr^{-1}$, while TU UMi appears to have a comparable rate of $0.3 \times 10^{-7} M_{\odot} yr^{-1}$. The primary masses of samples (M_1) in Tab. 4 apparently show no relationship with the period-change rate (dP/dt). However, there is the same relation between the secondary masses (M_2) and the period-change rate (dP/dt), where dP/dt decreases with increasing q. This is understandable because, in the study of Latković et al. (2021b), the empirical relationship between the secondary masses and the mass ratio shows a linear correlation, M_2 increases with increasing q. Most of the systems in Tab. 4 have a confirmed cyclic change related to the magnetic activity of components, or LTTE in the system. Although we accept that the long-term period decrease is due to conservative mass transfer between components, the contribution of angular momentum loss (AML) via magnetic stellar wind, or by a combination of both processes, on the secular period reducing cannot be ruled out. The cyclic OC variation can be explained in terms of the LTTE or solar-like magnetic activity cycle of one of the two components in the system. However, we can not discriminate which mechanism is responsible for the cyclic variation in the OC diagram and it is clear that we need more observations to ascertain that.

Acknowledgements. The authors acknowledge generous allotments of observing time at the Ege University Observatory. We thank S. Evren and G. Taş for their support in performing observations at the Ege University Observatory and the staff of the Ege University Observatory. We would like to thank Burak Ulaş for allowing us to use his python code to determine times of minima from TESS observations. And we thank the referee very much for the comments and suggestions that have helped us to improve the manuscript. This paper includes data collected by the TESS mission, which are publicly available from the Mikulski Archive for Space Telescopes (MAST). This research has made use of the SIMBAD online database, operated at CDS, Strasbourg, France, and NASAs Astrophysics Data System (ADS).

References

Applegate, J. H., A Mechanism for Orbital Period Modulation in Close Binaries. 1992, *Astrophysical Journal*, **385**, 621, DOI: 10.1086/170967

Bradstreet, D. H. & Guinan, E. F., Stellar Mergers and Acquisitions: The Formation and Evolution of W Ursae Majoris Binaries. 1994, in Astronomical Society of the Pacific Conference Series, Vol. **56**, *Interacting Binary Stars*, ed. A. W. Shafter, 228

Brát, L., Šmelcer, L., Kučáková, H., et al., B.R.N.O. Times of minima. 2008, *Open European Journal on Variable Stars*, **94**, 1

Budding, E. & Demircan, O. *Introduction to Astronomical Photometry*, , Vol. **6** (Cambridge University Pres)

Christopoulou, P. E., Papageorgiou, A., Vasileiadis, T., & Tsantilas, S., A Holistic View of the W UMa Type TY Boo. 2012, *Astronomical Journal*, **144**, 149, DOI: 10.1088/0004-6256/144/5/149

Christopoulou, P. E., Parageorgiou, A., & Chrysopoulos, I., First Modern Photometric Investigation of the Puzzling W UMa Type Close Binary System of TZ Bootis. 2011, *Astronomical Journal*, **142**, 99, DOI: 10.1088/0004-6256/142/4/99

Djurašević, G., Yılmaz, M., Baştürk, Ö., et al., Physical parameters of close binaries QX Andromedae, RW Comae Berenices, MR Delphini, and BD +079° 3142. 2011, *Astronomy and Astrophysics*, **525**, A66, DOI: 10.1051/0004-6361/201014895

Duerbeck, H. W., True and Possible Contact Binaries in the Hipparcos Catalogue. 1997, *Information Bulletin on Variable Stars*, **4513**

Gazeas, K. D., Physical parameters of contact binaries through 2-D and 3-D correlation diagrams. 2009, *Communications in Asteroseismology*, **159**, 129

He, J.-J., Wang, J.-J., & Qian, S.-B., V524 Monoceroits: A Marginal Contact Binary with a Cyclic Period Variation. 2012, *Publications of the ASJ*, **64**, 85, DOI: 10.1093/pasj/64.4.85

Hubscher, J., BAV-Results of observations - Photoelectric Minima of Selected Eclipsing Binaries and Maxima of Pulsating Stars. 2013, *Information Bulletin on Variable Stars*, **6084**, 1

Irwin, J. B., The Determination of a Light-Time Orbit. 1952, *Astrophysical Journal*, **116**, 211, DOI: 10.1086/145604

Kalytis, R., Three-channel general-purpose astrophotometer. 1999, *Turkish Journal of Physics*, **23**, 347

Kazarovets, E. V., Samus, N. N., Durlevich, O. V., et al., The 74th Special Name-list of Variable Stars. 1999, *Information Bulletin on Variable Stars*, **4659**

Kim, C.-H., Lee, J. W., Kim, S.-L., Han, W., & Koch, R. H., A Period Study and Light Synthesis for the W Ursae Majoris Type Binary SS Arietis. 2003, *Astronomical Journal*, **125**, 322, DOI: 10.1086/344808

Kjurkchieva, D., Dimitrov, D., & Ibryamov, S., BVR photometry of the star TU UMi. 2010, *Bulgarian Astronomical Journal*, **14**, 65

Kozai, Y., Secular perturbations of asteroids with high inclination and eccentricity. 1962, *Astronomical Journal*, **67**, 591, DOI: 10.1086/108790

Kriwattanawong, W. & Poojon, P., A photometric study of an EW-type binary system: GV Leo. 2013, *Research in Astronomy and Astrophysics*, **13**, 1330, DOI: 10.1088/1674-4527/13/11/004

Kwee, K. K. & van Woerden, H., A method for computing accurately the epoch of minimum of an eclipsing variable. 1956, *Bulletin of the Astronomical Institutes of the Netherlands,*, **12**, 327

Latković, O., Čeki, A., & Lazarević, S., Statistics of 700 Individually Studied W UMa Stars. 2021a, *Astrophysical Journal, Supplement*, **254**, 10, DOI: 10.3847/1538-4365/abeb23

Latković, O., Čeki, A., & Lazarević, S., Statistics of 700 Individually Studied W UMa Stars. 2021b, *Astrophysical Journal, Supplement*, **254**, 10, DOI: 10.3847/1538-4365/abeb23

Lee, J. W., Kim, S.-L., Lee, C.-U., & Youn, J.-H., The Solar-Type Contact Binary BX Pegasi Revisited. 2009, *Publications of the ASP*, **121**, 1366, DOI: 10.1086/649230

Lenz, P. & Breger, M., Period04 User Guide. 2005, *Communications in Asteroseismology*, **146**, 53, DOI: 10.1553/cia146s53

Li, M. C. A., Rattenbury, N. J., Bond, I. A., et al., A study of the light travel time effect in short-period MOA eclipsing binaries via eclipse timing. 2018, *Monthly Notices of the RAS*, **480**, 4557, DOI: 10.1093/mnras/sty2104

Li, Y.-Y., Li, K., & Liu, Y., The first photometric analysis and period investigation of the K-type W UMa type binary system V0842 Cep. 2021, *Research in Astronomy and Astrophysics*, **21**, 122, DOI: 10.1088/1674-4527/21/5/122

Liakos, A. & Niarchos, P., CCD Times of Minima of Several Eclipsing Binaries. 2010, *Information Bulletin on Variable Stars*, **5943**, 1

Liu, L., Qian, S. B., Liao, W. P., et al., Period Changes and Four-color Light Curves of the Active Overcontact Binary V396 Monocerotis. 2011, *Astronomical Journal*, **141**, 44, DOI: 10.1088/0004-6256/141/2/44

Liu, N. P., Qian, S. B., Soonthornthum, B., et al., The Late K-type Binary V1104 Her Near the Short-period End of Contact Binaries. 2015, *Astronomical Journal*, **149**, 148, DOI: 10.1088/0004-6256/149/4/148

Liu, Q.-Y. & Yang, Y.-L., On the Period Variation of the W UMa-type Contact Binary V502 Ophiuchi. 2006, *Chinese Journal of Astronomy and Astrophysics*, **6**, 331, DOI: 10.1088/1009-9271/6/3/08

Lu, H.-p., Zhang, L.-y., Michel, R., & Han, X. L., Magnetic Activity and Period Variation Studies of the Four W Uma-type Eclipsing Binaries: UV Lyn, V781 Tau, NSVS 4484038, and 2MASS J15471055+5302107. 2020, *Astrophysical Journal*, **901**, 169, DOI: 10.3847/1538-4357/abb19b

Maceroni, C., Milano, L., & Russo, G., Determination of parameters of W UMa systems. III : CC Com, YY Eri, V502 OPH and TY Pup. 1982, *Astronomy and Astrophysics, Supplement*, **49**, 123

Mitnyan, T., Bódi, A., Szalai, T., et al., The contact binary VW Cephei revisited: surface activity and period variation. 2018, *Astronomy and Astrophysics*, **612**, A91, DOI: 10.1051/0004-6361/201731402

Paczyński, B., Evolutionary Processes in Close Binary Systems. 1971, *Annual Review of Astron and Astrophys*, **9**, 183, DOI: 10.1146/annurev.aa.09.090171.001151

Pych, W. & Rucinski, S. M., TU UMi: A Contact Binary in a Triple System. 2004, *Information Bulletin on Variable Stars*, **5524**

Pych, W., Rucinski, S. M., DeBond, H., et al., Radial Velocity Studies of Close Binary Stars. IX. 2004, *Astronomical Journal*, **127**, 1712, DOI: 10.1086/382105

Qian, S., A period investigation of the overcontact binary system V417 Aquilae. 2003, *Astronomy and Astrophysics*, **400**, 649, DOI: 10.1051/0004-6361:20030018

Qian, S. & Yang, Y., Improved astrophysical parameters for the overcontact binary FG Hydrae. 2005, *Monthly Notices of the RAS*, **356**, 765, DOI: 10.1111/j.1365-2966.2004.08497.x

Qian, S. B., Liu, N. P., Liao, W. P., et al., First Photometric Investigation of the Newly Discovered W UMa-type Binary Star MR Com. 2013, *Astronomical Journal*, **146**, 38, DOI: 10.1088/0004-6256/146/2/38

Qian, S. B., Xiang, F. Y., Zhu, L. Y., et al., A New CCD Photometric Investigation of the Short-Period Close Binary AP Leonis. 2007, *Astronomical Journal*, **133**, 357, DOI: 10.1086/509499

Qian, S. B., Yang, Y. G., Soonthornthum, B., et al., Deep, Low Mass Ratio Overcontact Binary Systems. III. CU Tauri and TV Muscae. 2005, *Astronomical Journal*, **130**, 224, DOI: 10.1086/430673

Rodríguez, E., López-González, M. J., & López de Coca, P., A revised catalogue of delta Sct stars. 2000, *Astronomy and Astrophysics, Supplement*, **144**, 469, DOI: 10.1051/aas:2000221

Rolland, A., Costa, V., Rodriguez, E., et al., Is TU UMi a W UMa-type system. 2002, *Communications in Asteroseismology*, **142**, 57

Rucinski, S. M., Pych, W., Ogłoza, W., et al., Radial Velocity Studies of Close Binary Stars. X. 2005, *Astronomical Journal*, **130**, 767, DOI: 10.1086/431226

Sarotsakulchai, T., Qian, S.-B., Soonthornthum, B., et al., RW Doradus: A solar-type shallow contact binary with a new orbital period investigation. 2019a, *Publications of the ASJ*, **71**, 34, DOI: 10.1093/pasj/psy149

Sarotsakulchai, T., Qian, S.-B., Soonthornthum, B., et al., YZ Phoenicis: a very short period K-type contact binary with variation of the O'Connell effect and orbital period change. 2019b, *Publications of the ASJ*, **71**, 81, DOI: 10.1093/pasj/psz062

Schofield, M., Chaplin, W. J., Huber, D., et al., The Asteroseismic Target List for Solar-like Oscillators Observed in 2 minute Cadence with the Transiting Exoplanet Survey Satellite. 2019, *Astrophysical Journal, Supplement*, **241**, 12, DOI: 10.3847/1538-4365/ab04f5

Soydugan, F., Alicavus, F., Senyuz, T., et al., New CCD Minima Times for Selected Eclipsing Binaries. 2017, *Information Bulletin on Variable Stars*, **6225**, 1, DOI: 10.22444/IBVS.6225

Tran, K., Levine, A., Rappaport, S., et al., The Anticorrelated Nature of the Primary and Secondary Eclipse Timing Variations for the Kepler Contact Binaries. 2013, *Astrophysical Journal*, **774**, 81, DOI: 10.1088/0004-637X/774/1/81

Wang, J. J., Jiang, L. Q., Zhang, B., Zhao, S. Q., & Yu, J., Is There a Substellar Object Orbiting the Solar-like Stable Contact Binary V2284 Cyg? 2017, *Publications of the ASP*, **129**, 124202, DOI: 10.1088/1538-3873/aa8bb0

Xia, Q.-Q., Li, K., Chen, X., Guo, D.-F., & Gao, D.-Y., The first photometric investigation and period study of two W UMa-type binary systems: EF CVn and EH CVn. 2018, *Publications of the ASJ*, **70**, 104, DOI: 10.1093/pasj/psy103

Yang, Y. & Liu, Q., Period Changes of Two W UMa-Type Contact Binaries: RW Comae Berenices and CC Comae Berenices. 2003, *Publications of the ASP*, **115**, 748, DOI: 10.1086/374913

Yang, Y.-G., A photometric study of the K-type contact binary EI CVn. 2011, *Research in Astronomy and Astrophysics*, **11**, 181, DOI: 10.1088/1674-4527/11/2/006

Yang, Y. G., Wei, J. Y., & He, J. J., a Photometric Study of the Neglected Eclipsing Binary BS Cassiopeiae. 2008, *Astronomical Journal*, **136**, 594, DOI: 10.1088/0004-6256/136/2/594

Yang, Y.-G., Wei, J. Y., & Nakajima, K., On Period Variations of the K-Type Eclipsing Binary BM Ursae Majoris. 2009, *Publications of the ASJ*, **61**, 13, DOI: 10.1093/pasj/61.1.13

Zasche, P., Liakos, A., Niarchos, P., et al., Period changes in six contact binaries: WZ And, V803 Aql, DF Hya, PY Lyr, FZ Ori, and AH Tau. 2009, *New Astronomy*, **14**, 121, DOI: 10.1016/j.newast.2008.06.002

Zhang, X.-D. & Qian, S.-B., Orbital period cut-off of W UMa-type contact binaries. 2020, *Monthly Notices of the RAS*, **497**, 3493, DOI: 10.1093/mnras/staa2166

Zhang, Y., Han, Q. W., & Liu, J. Z., The First Photometric Study of the Short-period Shallow Contact System LO Comae. 2016, *Publications of the ASP*, **128**, 124201, DOI: 10.1088/1538-3873/128/970/124201

Zhou, X., Qian, S., Boonrucksar, S., et al., Photometric investigation of the contact binary GU Orionis with high metallicity. 2018, *Publications of the ASJ*, **70**, 87, DOI: 10.1093/pasj/psy084

Zhou, X. & Soonthornthum, B., Photometric investigation on the W-subtype contact binary V1197 Her. 2020, *Research in Astronomy and Astrophysics*, **20**, 010, DOI: 10.1088/1674-4527/20/1/10

Zhu, L. Y., Qian, S. B., Soonthornthum, B., et al., Three Close Binaries in Different Evolutionary Stages in the Old Open Cluster NGC 188. 2014, *Astronomical Journal*, **147**, 42, DOI: 10.1088/0004-6256/147/2/42

Zhu, L. Y., Qian, S. B., Soonthornthum, B., & Yang, Y. G., Deep, Low Mass Ratio Overcontact Binaries. II. IK Persei. 2005, *Astronomical Journal*, **129**, 2806, DOI: 10.1086/430187

Zhu, L. Y., Wang, Z. H., Tian, X. M., Li, L. J., & Gao, X., V1005 Her: a solar-type shallow-contact binary in a triply fossil system. 2019, *Monthly Notices of the RAS*, **489**, 2677, DOI: 10.1093/mnras/stz2294

Contrib. Astron. Obs. Skalnaté Pleso **52/2**, 25 – 43, (2022)
https://doi.org/10.31577/caosp.2022.52.2.25

Inverse problem of white dwarfs theory with rapid axial rotation

M. Vavrukh, D. Dzikovskyi and S. Smerechynskyi

Department of Astrophysics, Ivan Franko National University, Kyrylo & Methodiy str. 8, 79005 Lviv, Ukraine, (E-mail: mvavrukh@gmail.com)

Received: April 29, 2022; Accepted: September 9, 2022

Abstract. The objects of research are three recently discovered white dwarfs from binary systems with rapid axial rotation and masses $M \leq M_{\odot}$. The geometrical and mechanical characteristics (moment of inertia, equatorial gravity, the condition of stability in relation to rotation) are calculated for the white dwarf V1460 Her within an electron-nuclear model, based on the equilibrium equation and inferred from observations mass and period of axial rotation. Estimates of model parameters and macroscopic characteristics for inferred from observations periods of rotation are performed for white dwarfs LAMOST J024048.51+195226.9 and CTCV J2056-3014.

Key words: stars: white dwarfs – stars: rotation

1. Introduction

The traditional approach in the theory of white dwarfs with axial rotation is based on the Chandrasekhar model (Chandrasekhar, 1931) supplemented by solid body rotation (James, 1964; Roxburgh, 1965). The structure description of a white dwarf in this model is reduced to the mechanical equilibrium equation, which is a differential nonlinear equation of the second order in partial derivatives with two independent dimensionless parameters (the relativistic parameter in the stellar center x_0 and dimensionless angular velocity Ω). The solutions of the mechanical equilibrium equation for a fixed value of x_0 exist in the region $0 \leq \Omega \leq \Omega_{\max}(x_0)$ and give the opportunity to qualitatively determine the influence of rotation on white dwarfs' characteristics. All macroscopic characteristics of white dwarfs are functions of these two parameters. Angular velocity is one of the independent parameters to be used in more accurate models, which take into account finite temperature effects (incomplete degeneracy of an electron subsystem), Coulomb interparticle interactions, and magnetic fields (Tassoul, 1978). This approach does not refer to a specific dwarf, but to dwarfs in general.

Due to the development of methods of astronomical observations and technical equipment in recent years it yielded reliable data about white dwarfs in binary systems, in particular about their axial rotation and also in some cases

about their masses (Ashley et al., 2020). This gives an opportunity to formulate a new approach for calculations of the structure and characteristics of white dwarfs in binary systems. Namely, to solve the equilibrium equation for the specific white dwarf with inferred from observations angular velocity ω. In this case the dimensionless angular velocity Ω becomes a function of the relativistic parameter x_0, and the number of independent parameters in the equilibrium equation is reduced by one. This simplifies the inverse problem of theory – determination for observation data of other parameters of the model, as well as characteristics of white dwarfs, which are not determined from observed data.

For calculation of white dwarfs' structure we use the electron-nuclear model with a completely degenerate electron subsystem, which takes into account axial rotation and Coulomb interparticle interactions. The purpose of our work is to calculate geometrical and mechanical characteristics of the white dwarf V1460 Her (Ashley et al., 2020) for its mass and period of rotation as inferred from observations, as well as assessments of characteristics of LAMOST J024048.51+195226.9 (Pelisoli et al., 2021) and CTCV J2056-3014 only for inferred from observations periods of axial rotation (Lopes de Oliveira et al., 2020).

2. The equilibrium equation of white dwarf

In the standard approach, the equilibrium equation of a white dwarf with a constant angular velocity in a non-inertial reference frame is written in the form (James, 1964)

$$\nabla P(\mathbf{r}) = -\rho(\mathbf{r})\big\{\nabla\Phi_{\rm grav}(\mathbf{r}) + \nabla\Phi_{\rm c}(\mathbf{r})\big\}, \tag{1}$$

where

$$\rho(\mathbf{r}) = \frac{m_u\mu_e}{3\pi^2}\left(\frac{m_e c}{\hbar}\right)^3 x^3(\mathbf{r}) \tag{2}$$

is the density of matter, practically concentrated in nuclei, m_u is the atomic mass unit, m_e is the electron mass, c is the speed of light,

$$x(\mathbf{r}) \equiv \frac{\hbar}{m_e c}\big(3\pi^2 n_e(\mathbf{r})\big)^{1/3} \tag{3}$$

is the local value of a relativistic parameter, $n_e(\mathbf{r})$ is the number density of electrons at the point with the radius-vector $\mathbf{r}$, and $\mu_e = \langle A/z\rangle$ is the ratio of mass number of nucleus A to its charge z averaged over the volume of a star, therefore $\mu_e \approx 2.0$. In equation (1)

$$\Phi_{\rm grav}(\mathbf{r}) = -G\int\frac{\rho(\mathbf{r}')d\mathbf{r}'}{|\mathbf{r}-\mathbf{r}'|} \tag{4}$$

is the gravitational potential inside of a white dwarf. In the spherical coordinate system, whose axis Oz coincides with the axis of star' rotation, the centrifugal

potential is

$$\Phi_{\rm c}(\mathbf{r}) = -\frac{1}{2}\omega^2 r^2 \sin^2\theta, \tag{5}$$

where θ is the polar angle, and ω is the angular velocity. In the model which we use

$$P(\mathbf{r}) = P_0(\mathbf{r}) + P_{\rm int}(\mathbf{r}), \tag{6}$$

where

$$\begin{aligned} &P_0(\mathbf{r}) = \frac{\pi m_e^4 c^5}{3h^3}\mathcal{F}(x(\mathbf{r})),\\ &\mathcal{F}(x) = x(2x^2-3)[1+x^2]^{1/2} + 3\ln[x+(1+x^2)^{1/2}] \end{aligned} \tag{7}$$

is the pressure of an ideal relativistic completely degenerate electron subsystem within special theory of relativity, and $P_{\rm int}(\mathbf{r})$ is the contribution of Coulomb interparticle interactions. The nuclear subsystem is static, as in the Chandrasekhar model. The contribution to pressure in a spatially homogeneous electron-nuclear model is an expansion in powers of the fine-structure constant $\alpha_0 = e^2/\hbar c$, which was calculated in the work of Vavrukh et al. (2018),

$$\begin{aligned} &P_{\rm int} = -\frac{\pi m_e^4 c^5}{3h^3} f(x|z),\\ &f(x|z) = \alpha_0\left\{\frac{2}{\pi} + \frac{4d_0}{3\gamma}z^{2/3}\right\}x^4 - \frac{8}{3}\alpha_0^2\left\{\frac{d\mathcal{E}_{\rm cor}(x)}{dx} + z^{4/3}\frac{d\mathcal{E}_2(x|z)}{dx}\right\}x^4 + \ldots, \end{aligned} \tag{8}$$

which generalizes the expression obtained by Salpeter (1961). Here $\gamma = (9\pi/4)^{1/3}$, and x is the relativistic parameter in a homogeneous model. The parameter d_0 depends on the spatial distribution of nuclei: for the Wigner-Seitz cell (Pines & Noziéres, 1966) $d_0 = 1.8$; for a spatial cubic lattice $d_0 = 1.76$; for a hexagonal closest packing $d_0 = 1.79168$; and for cubic face-centered and body-centered configuartions $d_0 = 1.79186$ and 1.79172, respectively (Fuchs, 1935; Carr, 1961). The function $f(x|z)$ is positive, therefore, Coulomb interparticle interactions decrease the pressure. Axial rotation and Coulomb interparticle interactions are competing factors. The transition to a spatially inhomogeneous model is carried out by the substitution $x \to x(\mathbf{r})$ in formulae (8), which corresponds to the local approximation.

3. Model with axial rotation

Axial rotation and Coulomb interparticle interactions play the role of corrections and can be taken into account within the perturbation theory. These two factors are competing, so it is advisable to study their influence on the white dwarf characteristics separately. At the first stage we consider a model with rotation without Coulomb interparticle interactions. Substituting $P_0(\mathbf{r})$ and $\rho(\mathbf{r})$ in equation (1) we obtain a nonlinear differential equation for the relativistic

parameter $x(\mathbf{r})$. To obtain it in the form which is typical for the equation in the polytropic theory of stars, we introduce the dimensionless variables

$$\xi = r/\lambda(x_0), \quad Y(\xi,\theta) = \varepsilon_0^{-1}\big\{[1+x^2(\mathbf{r})]^{1/2} - 1\big\}, \tag{9}$$

where $\varepsilon_0 \equiv \varepsilon_0(x_0) = (1+x_0^2)^{1/2} - 1$, and the parameter $x_0 = x(\mathbf{r}=0)$ is determined by the number density of electrons in the stellar center according to definition (3). In these variables the equilibrium equation takes the form

$$\Delta_{\xi,\theta} Y(\xi,\theta) = \Omega^2 - \left\{ Y^2(\xi,\theta) + \frac{2}{\varepsilon_0} Y(\xi,\theta) \right\}^{3/2}, \tag{10}$$

where the Laplacian in variables (ξ,θ) equals

$$\Delta_{\xi,\theta} = \Delta_\xi + \frac{1}{\xi^2}\Delta_\theta, \ \Delta_\xi = \frac{1}{\xi^2}\frac{\partial}{\partial\xi}\left(\xi^2\frac{\partial}{\partial\xi}\right), \ \Delta_\theta = \frac{\partial}{\partial t}(1-t^2)\frac{\partial}{\partial t}, \ t = \cos\theta. \tag{11}$$

Herewith the scale length $\lambda(x_0)$ and dimensionless angular velocity Ω are determined by relations

$$\begin{aligned} &\frac{32\pi^2 G}{3(hc)^3}\big\{m_u\mu_e m_e c^2 \lambda(x_0)\varepsilon_0\big\}^2 = 1, \\ &\Omega = 2^{1/2}\omega\lambda(x_0)\left(\frac{m_u\mu_e}{m_e c^2\varepsilon_0}\right)^{1/2}. \end{aligned} \tag{12}$$

From first equality (12) we find that $\lambda(x_0) = R_0(\mu_e\varepsilon_0)^{-1}$, where

$$R_0 = \left(\frac{3}{2}\right)^{1/2}\frac{1}{4\pi}\left(\frac{h^3}{cG}\right)^{1/2}\frac{1}{m_0 m_u} \approx 0.776885{\cdot}10^9\,\text{cm} \approx 1.11623{\cdot}10^{-2} R_\odot \tag{13}$$

is the scale of white dwarfs' radii. From second expression (12) we have

$$\Omega = \frac{\omega}{\omega_0}\left(\frac{2}{\mu_e}\right)^{1/2}\varepsilon_0^{-3/2}, \ \omega_0 = \left(\frac{GM_0}{R_0^3}\right)^{1/2}. \tag{14}$$

Here

$$M_0 = \left(\frac{3}{2}\right)^{1/2}\frac{1}{4\pi}\left(\frac{hc}{G}\right)^{3/2}\frac{1}{m_u^2} \approx 5.740247\cdot 10^{33}\,\text{g} \approx 2.886649 M_\odot \tag{15}$$

is the scale of stellar masses and $\omega_0 \approx 0.9062\,\text{c}^{-1}$ is the scale of angular velocities.

According to definition (9), equation (10) corresponds to the boundary condition $Y(0,\theta) = 1$, and $\partial Y(\xi,\theta)/\partial\xi = 0$ at $\xi \Rightarrow 0$ is the condition for regularity of the solution. In equation (10) there appear two dimensionless parameters (x_0 and Ω). In our work (Vavrukh et al., 2022) we obtained solutions of equation

(10) in a linear approximation for Ω^2 in the region ($1 \le x_0 \le 24; 0 \le \Omega \le \Omega(x_0)$) and calculated polar and equatorial radii. Also we studied the shape of a white dwarf and calculated its mass, moment of inertia, equatorial gravity and total energy as functions of parameters x_0 and Ω.

But in the case when we know the angular velocity ω from observations, the dimensionless angular velocity determined by formula (14) is no longer an independent parameter – it becomes a function of parameters μ_e and x_0, $\Omega \equiv \Omega(x_0, \mu_e)$. At homogeneous chemical composition ω is actually a function of the parameter x_0. Methods of finding solutions of equation (10) at $\Omega \equiv \Omega(x_0)$ are the same as in the work of Vavrukh et al. (2022).

In the inner stellar region the solution of equation (10) is presented in the form

$$Y_I(\xi, \theta) = y(\xi) + \Omega^2 \Psi(\xi, \theta), \tag{16}$$

where $y(\xi)$ is the solution of the equilibrium equation at $\Omega = 0$

$$\Delta_\xi y(\xi) = -\left(y^2(\xi) + \frac{2}{\varepsilon_0} y(\xi)\right)^{3/2} \tag{17}$$

and satisfies the boundary conditions $y(0) = 1$, $\partial y(\xi)/\partial \xi = 0$ at $\xi = 0$. The condition $y(\xi) = 0$ determines the dimensionless radius of a white dwarf in the Chandrasekhar model $\xi_1(x_0)$. In the inner region, where $0 \le \xi \le \xi_1(x_0)$, the function $\Psi(\xi, \theta)$ can be considered as a correction and linearizes equation (10) relative to $\Psi(\xi, \theta)$. In such approximation this function satisfies the equation

$$\begin{aligned} &\Delta_{\xi,\theta} \Psi(\xi, \theta) = 1 - \Phi(\xi|x_0)\Psi(\xi, \theta), \\ &\Phi(\xi|x_0) = 3\left\{y(\xi) + \frac{1}{\varepsilon_0}\right\}\left\{y^2(\xi) + \frac{2}{\varepsilon_0} y(\xi)\right\}^{1/2}. \end{aligned} \tag{18}$$

Its solution can be represented in the form of expansions for the Legendre polynomials

$$\Psi(\xi, \theta) = \psi_0(\xi|x_0) + \sum_{l \ge 1} a_{2l}(x_0) P_{2l}(t) \psi_{2l}(\xi|x_0), \tag{19}$$

where $a_{2l}(x_0)$ are integration constants. The unknown functions satisfy the following ordinary linear equations

$$\begin{aligned} &\Delta_\xi \psi_0(\xi|x_0) = 1 - \Phi(\xi|x_0)\psi_0(\xi|x_0), \\ &\Delta_\xi \psi_{2l}(\xi|x_0) = \left\{\frac{2(2l+1)}{\xi^2} - \Phi(\xi|x_0)\right\}\psi_{2l}(\xi|x_0), \ l \ge 1. \end{aligned} \tag{20}$$

Equations (20) correspond to the boundary conditions $\psi_{2l}(\xi|x_0) = 0$, $\partial \psi_{2l}(\xi|x_0)/\partial \xi = 0$ at $\xi \to 0$ for all $l \ge 0$. The function $\psi_0(\xi|x_0)$ has asymptotics $\xi^2/6 + \ldots$ at $\xi \ll 1$. Functions $\psi_{2l}(\xi|x_0)$ at $\xi \ll 1$ have asymptotics of a spherical Bessel function, so we use a normalization for them

$$\psi_{2l}(\xi|x_0) \Rightarrow \{(4l+1)!!\}^{-1} \xi^{2l} + \ldots \ \text{ at } \ \xi \ll 1. \tag{21}$$

In the region of stellar periphery ($\xi > \xi_1(x_0)$), where $Y(\xi,\theta)$ has a small value, the solution of equation (10) is close to the solution of

$$\Delta_{\xi,\theta} Y_{II}(\xi,\theta) = \Omega^2 - \left(\frac{2}{\varepsilon_0}\right)^{3/2} Y_{II}^{3/2}(\xi,\theta), \tag{22}$$

which is similar to the equation of a rotating polytrope with index $n = 1.5$. By the method of successive approximations we find that

$$\begin{aligned} Y_{II}(\xi,\theta) &= \frac{\xi^2\Omega^2}{4}(1-t^2) - \left(\frac{2}{\varepsilon_0}\right)^{3/2} \frac{\xi^5\Omega^3}{25}(1-t^2)^{5/2} + \dots \\ &+ \Omega^2 \sum_{l=0}^{2} \left\{ c_{2l}(x_0)\xi^{2l} P_{2l}(t) + b_{2l}(x_0)\frac{P_{2l}(t)}{\xi^{2l+1}} \right\}, \end{aligned} \tag{23}$$

where $c_{2l}(x_0)$, $b_{2l}(x_0)$ are integration constants.

Solutions of equations (20) are found numerically. To find integration constants $a_{2l}(x_0)$ we use the integral form of the equilibrium equation

$$Y_I(\xi,\theta) = 1 + \frac{\xi^2\Omega^2}{6}\Big(1 - P_2(t)\Big) + \frac{1}{4\pi}\int Q(\boldsymbol{\xi},\boldsymbol{\xi}')\left\{ Y_I^2(\xi',\theta') + \frac{2}{\varepsilon_0} Y_I(\xi',\theta') \right\}^{3/2} d\boldsymbol{\xi}', \tag{24}$$

which contains the kernel

$$Q(\boldsymbol{\xi},\boldsymbol{\xi}') = |\boldsymbol{\xi} - \boldsymbol{\xi}'|^{-1} - (\xi')^{-1}, \tag{25}$$

and integration is performed over the entire stellar volume. The surface of a rotating white dwarf is close to the surface of a rotational ellipsoid. To find integration constants we use the method of successive approximations. We restrict ourselves to integrating over the inner part of a rotational ellipsoid $\xi \le \xi_1(x_0)$ (the unshaded region in Fig. 1, where $\xi_p(x_0)$ is the polar radius, and $\xi_e(x_0)$ is the equatorial one) to find constants $a_{2l}(x_0)$. Substituting expressions (16), (19) for $Y(\xi',\theta')$ in equation (24) and linearizing the subintegral function relative to Ω^2, we obtain

$$\begin{aligned} & y(\xi|x_0) + \Omega^2 \left\{ \psi_0(\xi|x_0) + \sum_{l\ge 1} a_{2l}(x_0) P_{2l}(t)\psi_{2l}(\xi|x_0) \right\} = \\ & = 1 + \frac{\xi^2\Omega^2}{6}\Big(1 - P_2(t)\Big) + \frac{1}{4\pi}\int Q(\boldsymbol{\xi},\boldsymbol{\xi}')\times \\ & \times \left\{ \left[y^2(\xi'|x_0) + \frac{2}{\varepsilon_0} y(\xi'|x_0) \right]^{3/2} + \Omega^2 \Phi(\xi'|x_0)\times \right. \\ & \left. \times \left[\psi_0(\xi'|x_0) + \sum_{l\ge 1} a_{2l}(x_0) P_{2l}(t')\psi_{2l}(\xi'|x_0) \right] \right\} d\boldsymbol{\xi}'. \end{aligned} \tag{26}$$

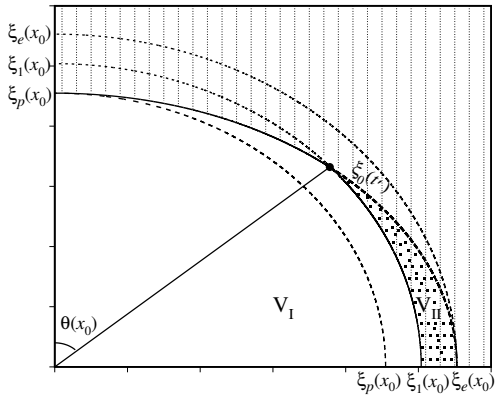

Figure 1. A schematic representation of the quarter part of the meridional section of a white dwarf.

The region of integration is determined by

$$\begin{aligned} &0 \le \xi' \le \xi_0(t') \quad \text{at} \quad 1 \ge |t'| \ge t(x_0); \quad t(x_0) = \cos\theta(x_0), \\ &0 \le \xi' \le \xi_1(x_0) \quad \text{at} \quad 0 \le |t'| \le t(x_0), \end{aligned} \tag{27}$$

where the polar angle $\theta(x_0)$ is determined by the intersection of Chandrasekhar sphere and the ellipsoid surface $\xi_0(t')$, therefore

$$\xi_p(x_0)\{1 - e^2(x_0)[1 - t^2(x_0)]\}^{-1/2} \approx \xi_1(x_0), \tag{28}$$

where $e(x_0)$ is the eccentricity of the ellipsoid, $\xi_e(x_0)$, $\xi_p(x_0)$ and $e(x_0)$ depend on Ω and are determined self-consistently. The outer region of the ellipsoid (darkened) is given by

$$\xi_1(x_0) \le \xi' \le \xi_0(t') \quad \text{at} \quad 0 \le |t'| \le t(x_0). \tag{29}$$

Using the integral form of equations for functions $y(\xi')$ and $\psi_0(\xi'|x_0)$, it is possible to cast equation (26) to such form, that does not contain terms of type $a_{2l}(x_0)P_{2l}(t)\psi_{2l}(\xi|x_0)$ (they are cancel each other), and equation (26) acquires the form

$$\begin{aligned} &\sum_{l\ge1} P_{2l}(t)\xi^{2l}\left\{a_{2l}(x_0)S_{2l,2l}(x_0) + \sum_{m\ge1}(1-\delta_{m,l})a_{2m}(x_0)S_{2m,2l}(x_0)\right\} = \\ &= -\frac{\xi^2}{6}P_2(t) - \sum_{l\ge1} P_{2l}(t)\xi^{2l}\left\{\frac{I_{2l}(x_0)}{2} + \frac{L_{2l}(x_0)}{\Omega^2} + D_{2l}(x_0)\right\}. \end{aligned} \tag{30}$$

According to orthogonality of the Legendre polynomials from equality (30) we find the system of algebraic equations for integration constants

$$\begin{aligned}
&a_2(x_0)S_{2,2}(x_0) + \sum_{m\geq 2} a_{2m}(x_0)S_{2m,2}(x_0) = \\
&= -\frac{1}{6}\Big(1 + 3I_2(x_0)\Big) - \frac{L_2(x_0)}{\Omega^2} - D_2(x_0), \\
&a_{2l}(x_0)S_{2l,2l}(x_0) + \sum_{m\geq 1} a_{2m}(x_0)(1-\delta_{m,l})S_{2m,2l}(x_0) = \\
&= -\frac{I_{2l}(x_0)}{2} - \frac{L_{2l}(x_0)}{\Omega^2} - D_{2l}(x_0)
\end{aligned} \tag{31}$$

at $l \geq 2$. In formulae (30), and (31) introduced the following notations

$$\begin{aligned}
&S_{2l,2m}(x_0) = \int\limits_{t(x_0)}^{1} P_{2l}(t')P_{2m}(t')dt' \int\limits_{\xi_0(t')}^{\xi_1(x_0)} (\xi')^{1-2m}\times \\
&\times\left\{\frac{2l(l+1)}{(\xi')^2}\psi_{2l}(\xi'|x_0) - \Delta_{\xi'}\psi_{2l}(\xi'|x_0)\right\}d\xi', \\
&S_{2l,2l}(x_0) = (4l+1)^{-1}\xi_1^{-2l}\left\{(2l+1)\psi_{2l}(\xi_1|x_0) + \xi_1\frac{d\psi_{2l}(\xi_1|x_0)}{d\xi_1}\right\} + \\
&+ \int\limits_{t(x_0)}^{1} P_{2l}^2(t)\Big\{\xi_0^{-2l}\left[(2l+1)\psi_{2l}(\xi_0|x_0) + \xi_0\frac{d\psi_{2l}(\xi_0|x_0)}{d\xi_0}\right] - \\
&- \xi_1^{-2l}\left[(2l+1)\psi_{2l}(\xi_1|x_0) + \xi_1\frac{d\psi_{2l}(\xi_1|x_0)}{d\xi_1}\right]\Big\}\,dt, \\
&L_{2l}(x_0) = \int\limits_{t(x_0)}^{1} P_{2l}(t')dt' \int\limits_{\xi_0(t')}^{\xi_1(x_0)} (\xi')^{1-2l}\left\{y^2(\xi'|x_0) + \frac{2}{\varepsilon_0}y(\xi'|x_0)\right\}^{3/2} d\xi', \\
&D_{2l}(x_0) = \int\limits_{t(x_0)}^{1} dt' P_{2l}(t') \int\limits_{\xi_0(t')}^{\xi_1(x_0)} (\xi')^{1-2l}\big\{\Delta_{\xi'}\psi_0(\xi'|x_0)\big\}dt', \\
&I_2(x_0) = -2\int\limits_{t(x_0)}^{1} P_2(t')\{\ln\xi_0(t') - \ln\xi_1(x_0)\}dt', \\
&I_{2l}(x_0) = (l-1)^{-1}\int\limits_{t(x_0)}^{1} P_{2l}(t')\{[\xi_0(t')]^{2-2l} - [\xi_1(x_0)]^{2-2l}\}dt'.
\end{aligned} \tag{32}$$

We have two representations of the equilibrium equation solution: in the inner region representation (16), in periphery – (23). Integration constants $c_{2l}(x_0)$, $b_{2l}(x_0)$ are determined from the continuity condition on the sphere $\xi_1(x_0)$ at $0 \le |t| \le t(x_0)$. In this part of the sphere $|t|$ has a small value, therefore $42(1-t^2)^{5/2} \simeq 13 - 25P_2(t) + 18P_4(t) + \ldots$. In the approach to $P_4(t)$ inclusive, integration constants are determined by the following relations

$$
\begin{aligned}
c_0(x_0) &= \xi_1 \frac{y'(\xi_1)}{\Omega^2} + \left\{ \psi_0(\xi_1) - \frac{\xi_1^2}{2} + \xi_1 \psi_0'(\xi_1) \right\} + \frac{13}{175} \left(\frac{2}{\varepsilon_0} \right)^{3/2} \Omega \xi_1^5; \\
b_0(x_0) &= \xi_1 \left\{ \psi_0(\xi_1) - \frac{\xi_1^2}{6} - c_0(x_0) + \frac{13}{42 \cdot 25} \left(\frac{2}{\varepsilon_0} \right)^{3/2} \Omega \xi_1^5 \right\}; \\
c_2(x_0) &= \frac{1}{6} + \frac{a_2(x_0)}{5\xi_1^2} \left\{ 3\psi_2(\xi_1) + \xi_1 \psi_2'(\xi_1) \right\} - \frac{4}{5 \cdot 21} \left(\frac{2}{\varepsilon_0} \right)^{3/2} \Omega \xi_1^3; \\
b_2(x_0) &= \xi_1^3 \left\{ a_2(x_0) \psi_2(\xi_1) + \frac{\xi_1^2}{6} - c_2(x_0) \xi_1^2 - \frac{1}{42} \left(\frac{2}{\varepsilon_0} \right)^{3/2} \Omega \xi_1^5 \right\}; \\
c_4(x_0) &= \frac{1}{9\xi_1^4} \left\{ a_4(x_0) [5\psi_4(\xi_1) + \xi_1 \psi_4'(\xi_1)] + \frac{6}{35} \left(\frac{2}{\varepsilon_0} \right)^{3/2} \Omega \xi_1^5 \right\}; \\
b_4(x_0) &= \xi_1^5 \left\{ a_4(x_0) \psi_4(\xi_1) - c_4(x_0) \xi_1^4 + \frac{3}{175} \left(\frac{2}{\varepsilon_0} \right)^{3/2} \Omega \xi_1^5 \right\}.
\end{aligned}
\tag{33}
$$

In formulae (33) $\xi_1 \equiv \xi_1(x_0)$, $y'(\xi_1) \equiv \partial y(\xi_1)/\partial \xi_1$, $\psi_{2l}'(\xi_1) \equiv \partial \psi_{2l}(\xi_1|x_0)/\partial \xi_1$, $\psi_{2l}(\xi_1) \equiv \psi_{2l}(\xi_1|x_0)$.

Systems of equations (31) and (33) are not independent because the coefficients (32) depend on the form of white dwarf's surface $\xi_0(t)$ determined by solutions (16) and (23). Therefore, systems of equations (31) and (33) should be solved by a self-consistent method of iterations. In the zero approximation for the surface of a rotating white dwarf we accept the Chandrasekhar sphere ($\xi_0(t) = \xi_1(x_0)$). In this approximation only $S_{2l,2l}(x_0)$ are non-zero, and constant $a_2^{(0)}(x_0)$ is determined by

$$
a_2^{(0)}(x_0) = -\{6S_{2,2}^{(0)}(x_0)\}^{-1} = -\frac{5}{6}\xi_1^2(x_0) \left\{ 3\psi_2(\xi_1|x_0) + \xi_1 \psi_2'(\xi_1|x_0) \right\}^{-1} \tag{34}
$$

and does not depend on the angular velocity Ω. All other constants $a_{2l}^{(0)}(x_0)$ at $l \ge 2$ are zero. This approximation corresponds to the Milne-Chandrasekhar (Milne, 1923; Chandrasekhar, 1933) approximation in the polytropes theory and is applicable for small angular velocities. In this approximation we find $c_0^{(0)}(x_0)$, $b_0^{(0)}(x_0)$, $c_2^{(0)}(x_0)$, $b_2^{(0)}(x_0)$ by expressions (33). Found in this way constants determined the zero approximation of functions (16) and (23). The surface of a rotating white dwarf is close to the surface of a rotational ellipsoid. Therefore in the subsequent iteration of $\xi_0(t)$ we adopt the surface of such ellipsoid, whose

polar and equatorial radii are determined from functions (16) and (23) in the zero approximation. In this case, the coefficients $I_{2l}(x_0)$, $L_{2l}(x_0)$, $D_{2l}(x_0)$ and $S_{2m,2l}(x_0)$ at $l \geq 1$ are already non-zero, the functions $S_{2l,2l}(x_0)$ are being specified. From system (31) we determine constants $a_2^{(1)}(x_0)$, $a_4^{(1)}(x_0)$, which makes it possible to find constants $b_{2l}^{(1)}(x_0)$, $c_{2l}^{(1)}(x_0)$ and specify the surface equation $\xi_0(t)$ etc. It is enough to perform 4-5 iterations. As a result we obtain functions (16) and (23) with integration constants depending on x_0 and ω, which determine the shape of the white dwarf's surface, not only the polar and equatorial radii

$$R_p(x_0|\omega) = \frac{R_0}{\mu_e \varepsilon_0}\xi_p(x_0|\omega), \quad R_e(x_0|\omega) = \frac{R_0}{\mu_e \varepsilon_0}\xi_e(x_0|\omega). \tag{35}$$

Herewith $\xi_p(x_0|\omega)$ is determined by condition $Y_I(\xi, 0) = 0$ and $\xi_e(x_0|\omega)$ – by condition $Y_{II}(\xi, \pi/2) = 0$. The stellar surface $\xi_0(t)$ is determined by conditions

$$\begin{aligned} &Y_I(\xi, \theta) = 0 \quad \text{at} \quad 1 \geq |t| \geq t(x_0), \\ &Y_{II}(\xi, \theta) = 0 \quad \text{at} \quad t(x_0) \geq |t| \geq 0. \end{aligned} \tag{36}$$

The volume of a white dwarf equals

$$V(x_0|\omega) = \frac{4\pi}{3}\left\{\frac{R_0}{\mu_e}\right\}^3 v(x_0|\omega), \quad v(x_0|\omega) = \frac{1}{\varepsilon_0^3}\int\limits_0^1 \xi_0^3(t)dt. \tag{37}$$

Its mass is determined by integration of the density $\rho(\mathbf{r})$ over the volume

$$\begin{aligned} M(x_0|\omega) &= \frac{M_0}{\mu_e^2}\mathcal{M}(x_0|\omega), \\ \mathcal{M}(x_0|\omega) &= \int\limits_0^1 dt \int\limits_0^{\xi_0(t)} \xi^2 \left\{Y^2(\xi, \theta) + \frac{2}{\varepsilon_0}Y(\xi, \theta)\right\}^{3/2} d\xi. \end{aligned} \tag{38}$$

The moment of inertia relative to the axis of rotation is

$$\begin{aligned} I(x_0|\omega) &= \int \rho(\mathbf{r}) r^2 \sin^2\theta d\mathbf{r} = \frac{M_0 R_0^2}{\mu_e^4}\mathcal{J}(x_0|\omega), \\ \mathcal{J}(x_0|\omega) &= \frac{1}{\varepsilon_0^2}\int\limits_0^1 (1 - t^2)dt \int\limits_0^{\xi_0(t)} \xi^4 \left\{Y^2(\xi, \theta) + \frac{2}{\varepsilon_0}Y(\xi, \theta)\right\}^{3/2} d\xi. \end{aligned} \tag{39}$$

The value of equatorial gravity is

$$\begin{aligned} &\frac{GM(x_0|\omega)}{R_e^2(x_0|\omega)} - \omega^2 R_e(x_0|\omega) = \frac{GM_0}{R_0^2}g_e(x_0|\omega), \\ &g_e(x_0|\omega) = \frac{\mathcal{M}(x_0|\omega)\varepsilon_0^2}{\xi_e^2(x_0|\omega)} - \frac{\omega^2}{\omega_0^2}\frac{\xi_e(x_0|\omega)}{\mu_e \varepsilon_0}. \end{aligned} \tag{40}$$

The total energy of a white dwarf is

$$E(x_0|\omega) = E_0(x_0|\omega) + E_{\rm grav}(x_0|\omega) + E_{\rm rot}(x_0|\omega), \tag{41}$$

where $E_0(x_0|\omega)$ is the kinetic energy of the electron subsystem, $E_{\rm grav}(x_0|\omega)$ is the gravitational energy of the nuclear subsystem, $E_{\rm rot}(x_0|\omega)$ is the energy of the rotation of a star as a whole. Using relations between the pressure $P_0(x)$ and the energy $E_0(x)$ of an ideal homogeneous electron subsystem (with a number of electrons N_e in a volume V)

$$P_0(x) = \left(\frac{m_0 c}{\hbar}\right)^3 (9\pi^2 N_e)^{-1} x^4 \, \frac{dE_0(x)}{dx}, \tag{42}$$

we can obtain the expression for the volume density of energy

$$\mathcal{E}_0(x) = \frac{E_0(x)}{V} = 3x^3 \int\limits_0^x \frac{ds}{s^4} P_0(s) = \frac{\pi m_0^4 c^5}{3h^3}\left\{x^3[(1+x^2)^{1/2}-1] - \frac{1}{8}\mathcal{F}(x)\right\}. \tag{43}$$

The density of kinetic energy in an inhomogeneous model $\mathcal{E}(x(r))$ is obtained by substitution $x \to x(r)$ in formula (43), therefore

$$E_0(x_0|\omega) = \int \mathcal{E}_0(x(\mathbf{r}))d\mathbf{r} = \frac{E_0}{\mu_e^3 \varepsilon_0^3}\frac{1}{4\pi}\int\limits_V \left\{x^3(\boldsymbol{\xi})[(1+x^2(\boldsymbol{\xi}))^{1/2}-1] - \frac{1}{8}\mathcal{F}(x(\boldsymbol{\xi}))\right\} d\boldsymbol{\xi},$$

$$x(\boldsymbol{\xi}) = \varepsilon_0\left\{Y^2(\xi,\theta) + \frac{2}{\varepsilon_0}Y(\xi,\theta)\right\}^{1/2} \equiv \varepsilon_0 X(\xi,\theta), \tag{44}$$

where

$$E_0 = G\frac{M_0^2}{R_0} = \left(\frac{3}{2}\right)^{1/2} \frac{1}{4\pi}\frac{h^{3/2}c^{7/2}m_0}{G^{3/2}m_u^3} \tag{45}$$

is the scale of energy.

According to formula (2) the gravitational energy can be represented in the form

$$E_{\rm grav}(x_0|\omega) = -\frac{E_0\varepsilon_0}{2\mu_e^3}(4\pi)^{-2}\iint\limits_V X^3(\xi_1,\theta_1)X^3(\xi_2,\theta_2)|\boldsymbol{\xi}_1 - \boldsymbol{\xi}_2|^{-1} d\boldsymbol{\xi}_1 d\boldsymbol{\xi}_2. \tag{46}$$

Using equation (24) and definition of kernel (25) we obtain the relation

$$\begin{aligned}
&(4\pi)^{-1}\int\limits_V X^3(\xi_2,\theta_2)|\boldsymbol{\xi}_1 - \boldsymbol{\xi}_2|^{-1} d\boldsymbol{\xi}_2 = \\
&= Y(\xi_1,\theta_1) - 1 + C(x_0|\omega) - \xi_1^2\omega^2(1 - P_2(t_1))(3\mu_e\omega_0^2\varepsilon_0^3)^{-1}, \\
&C(x_0|\omega) = (4\pi)^{-1}\int\limits_V X^3(\xi,\theta)\frac{d\boldsymbol{\xi}}{\xi}.
\end{aligned} \tag{47}$$

This allows us to represent $E_{\rm grav}(x_0|\omega)$ in the form of an integrals' sum by a vector $\boldsymbol{\xi}$

$$E_{\rm grav}(x_0|\omega) = -\frac{E_0\varepsilon_0}{2\mu_e^3}\Big\{(4\pi)^{-1}\int\limits_V Y(\xi,\theta)X^3(\xi,\theta)d\boldsymbol{\xi}+ \\ + [C(x_0|\omega)-1]\mathcal{M}(x_0|\omega) - \frac{\omega^2}{\mu_e\omega_0^2\varepsilon_0}\mathcal{J}(x_0|\omega)\Big\}. \tag{48}$$

The energy of rotation is

$$E_{\rm rot}(x_0|\omega) = \frac{E_0}{2\mu_e^4}\mathcal{J}(x_0|\omega)\frac{\omega^2}{\omega_0^2}. \tag{49}$$

3.1. Determination of model parameters and characteristics of white dwarfs according to the observed data

There are two parameters in the considered model – the relativistic parameter x_0 and the chemical composition parameter $\mu_e \approx 2.0$. The angular velocity ω compounds to its observed value. The mass of a white dwarf that is a component of a binary system can be determined from observations of orbital motions of components, using the Kepler law.

1. For the white dwarf V1460 Her there is known the period of rotation $P = 38.9\,\mathrm{s}$, which corresponds to the angular velocity $\omega = 0.162\,\mathrm{s}^{-1}$. The observed value of mass $M_{\rm obs} = 0.869M_\odot$ is given in the work of Ashley et al. (2020). In this case the inverse problem is completely defined, which allows us to determine the parameter x_0 for this white dwarf as a root of the equation

$$M_{\rm obs} = \frac{M_0}{\mu_e^2}\mathcal{M}(x_0|\omega), \tag{50}$$

where $\mathcal{M}(x_0|\omega)$ is determined by expressions (38). According to our calculations, this white dwarf corresponds to the model with the relativistic parameter

$$x_0 = 1.850 \quad \text{at} \quad \mu_e = 2.0. \tag{51}$$

The dimensionless values of characteristics calculated by formulae (35) – (49) are shown in Tab. 1. Herewith $\mathscr{E}(x_0|\omega)$ is the total energy of a white dwarf in units $E_0\mu_e^{-3}$. The values $\xi_p(x_0|\omega)$ and $\xi_e(x_0|\omega)$ correspond to the

Table 1. Characteristics of the white dwarf V1460 Her.

$\xi_p(x_0\|\omega)$	$\xi_e(x_0\|\omega)$	$\mathcal{M}(x_0\|\omega)$	$\mathcal{J}(x_0\|\omega)$	$g_e(x_0\|\omega)$	$\mathscr{E}(x_0\|\omega)$
1.9010	1.9891	1.20668	0.67521	0.341987	−0.308615

following parameters of the polar and equatorial radii

$$R_p(x_0|\omega) \cong 6.70 \cdot 10^3 \,\text{km}, \quad R_e(x_0|\omega) \cong 7.01 \cdot 10^3 \,\text{km}. \tag{52}$$

According to these data, we find the average matter density of a white dwarf

$$\bar{\rho} = M_{\text{obs}} \left\{ \frac{4}{3}\pi R_e^2(x_0|\omega) R_p(x_0|\omega) \right\}^{-1} = 1.258 \cdot 10^6 \,\text{g/cm}^3, \tag{53}$$

as well as the matter density in the stellar center according to formula (2)

$$\rho_{\text{c}} = \frac{m_u \mu_e}{3\pi^2} \left(\frac{m_e c}{\hbar} \right)^3 x_0^3 = 12.449 \cdot 10^6 \,\text{g/cm}^3. \tag{54}$$

The maximal (critical) angular velocity for this white dwarf stemming from the formula

$$\omega_{\max} = \left(\frac{G M_{\text{obs}}}{R_e^3} \right)^{1/2}, \tag{55}$$

equals $0.581\,\text{s}^{-1}$ and the ratio $\eta = \omega/\omega_{\max} = 0.279$.

2. For the white dwarf LAMOST J024048.51+195226.9 from observations there is known only the period of rotation $P = 25\,\text{s}$ (angular velocity $\omega = 0.251\,\text{s}^{-1}$), and its mass is unknown (Pelisoli et al., 2021). In this situation, there are not enough observed data for the accurate solution of the inverse problem. It is only possible to ascertain the parameter x_0 and characteristics of a white dwarf. The critical angular velocity is determined from formulae (40) at $g_e(x_0|\omega) = 0$

$$\omega_{\max} = \omega_0 \left\{ \frac{\mu_e \varepsilon_0^3 \mathcal{M}(x_0|\omega_{\max})}{\xi_e^3(x_0|\omega_{\max})} \right\}^{1/2}. \tag{56}$$

The angular velocity of this white dwarf is very high. Let us assume that it is close to the maximal value. Putting in equation (56) $\omega_{\max} = \omega$, we find the root of this equation

$$x_0 = 1.383 \quad \text{at} \quad \mu_e = 2.0. \tag{57}$$

This value of x_0 corresponds to the following values of characteristics

$$\begin{aligned} &\mathcal{M}(x_0|\omega) = 1.07886; \quad \mathcal{J}(x_0|\omega) = 1.1004; \\ &\xi_p(x_0|\omega) = 1.3732; \quad \xi_e(x_0|\omega) = 1.9422; \\ &M(x_0|\omega) = 0.779 M_\odot; \quad R_p \cong 7.56 \cdot 10^3 \,\text{km}; \quad R_e \cong 10.67 \cdot 10^3 \,\text{km}. \end{aligned} \tag{58}$$

The average matter density of a white dwarf and the matter density in the center equal $\bar{\rho} = 0.429 \cdot 10^6 \,\text{g/cm}^3$ and $\rho_{\text{c}} = 5.201 \cdot 10^6 \,\text{g/cm}^3$ respectively.

3. Analogous estimates we performed for the white dwarf CTCV J2056-3014 with the period of rotation $P = 29.6\,\mathrm{s}$ ($\omega = 0.212\,\mathrm{s}^{-1}$) (Lopes de Oliveira et al., 2020). In the approximation $\omega_{\max} = \omega$ we find that

$$\begin{aligned} &x_0 = 1.209 \quad \text{at} \quad \mu_e = 2.0; \\ &\mathcal{M}(x_0|\omega) = 0.966456; \quad \mathcal{J}(x_0|\omega) = 1.1843; \\ &\xi_p(x_0|\omega) = 1.1915; \quad \xi_e(x_0|\omega) = 1.7271; \\ &M(x_0|\omega) = 0.697 M_\odot; \quad R_p(x_0|\omega) \cong 8.14 \cdot 10^3\,\mathrm{km}; \\ &R_e(x_0|\omega) \cong 11.79 \cdot 10^3\,\mathrm{km}. \end{aligned} \tag{59}$$

For this white dwarf $\bar{\rho} = 0.293 \cdot 10^6\,\mathrm{g/cm}^3$, $\rho_\mathrm{c} = 3.475 \cdot 10^6\,\mathrm{g/cm}^3$.

4. Model with Coulomb interparticle interactions

Next, it is reasonable to consider the auxiliary model with Coulomb interparticle interactions but without axial rotation, putting $\omega = 0$ and using the equations of state (6)-(8). The model has spherical symmetry and three dimensionless parameters – x_0, μ_e and the nuclear charge $z \geq 2$. In variables

$$\xi = r/\lambda(x_0), \quad \tilde{y}(\xi|z) = \varepsilon_0^{-1}\{[1 + x^2(r)]^{1/2} - 1\} \tag{60}$$

the equilibrium equation is similar to equation (17)

$$\Delta_\xi \tilde{y}(\xi|z) = \hat{L}\tilde{y}(\xi|z) - \left\{\tilde{y}^2(\xi|z) + \frac{2}{\varepsilon_0}\tilde{y}(\xi|z)\right\}^{3/2}, \tag{61}$$

where

$$\begin{aligned} \hat{L}\tilde{y}(\xi|z) = \varphi_1(x|z)\Delta_\xi\left\{\tilde{y}^2(\xi|z) + \frac{2}{\varepsilon_0}\tilde{y}(\xi|z)\right\}^{1/2} + \\ + \varphi_2(x|z)\left\{\frac{d}{d\xi}\left[\tilde{y}^2(\xi|z) + \frac{2}{\varepsilon_0}\tilde{y}(\xi|z)\right]^{1/2}\right\}^2. \end{aligned} \tag{62}$$

Here we introduced the notation

$$\begin{aligned} &\varphi_1(x|z) = \frac{1}{8x^3}\frac{df(x|z)}{dx}, \quad \varphi_2(x|z) = \frac{\varepsilon_0}{8}\frac{d}{dx}\left\{\frac{1}{x^3}\frac{df(x|z)}{dx}\right\}, \\ &x \equiv x(\xi) = \varepsilon_0\left(\tilde{y}^2(\xi|z) + \frac{2}{\varepsilon_0}\tilde{y}(\xi|z)\right)^{1/2}. \end{aligned} \tag{63}$$

Equation (61) satisfies the same boundary conditions as equation (17). The root of equation $\tilde{y}(\xi|z) = 0$ determines the dimensionless radius of a star, $\xi_1(x_0|z)$,

in the scale $\lambda(x_0)$, therefore, expressions for the mass and radius are analogous to relations (35), (38),

$$R(x_0|z) = \frac{R_0}{\mu_e \varepsilon_0}\xi_1(x_0|z),\ M(x_0|z) = \frac{M_0}{\mu_e^2}\mathcal{M}(x_0|z),$$
$$\mathcal{M}(x_0|z) = \int\limits_0^{\xi_1(x_0|z)} \left\{\tilde{y}^2(\xi|z) + \frac{2}{\varepsilon_0}\tilde{y}(\xi|z)\right\}^{3/2} \xi^2 d\xi. \tag{64}$$

The solutions of equation (61) are found numerically in the region of the parameters $1 \le x_0 \le 3$; $2 \le z \le 12$. Dependence of the dimensionless mass $\mathcal{M}(x_0|z)$ and the dimensionless radius on the parameters $(x_0,\ z)$ are illustrated in Tab. 2. As it was shown in Table, the relative decrease of the mass due

Table 2. Dependence of the dimensionless mass $\mathcal{M}(x_0|z)$ and the dimensionless radius $\xi_1(x_0|z)$ on the parameters x_0 and z ($z = 0$ corresponds to the standard model).

x_0	$\mathcal{M}(x_0\|z)$				$\xi_1(x_0\|z)$			
	$z=0$	$z=2$	$z=6$	$z=12$	$z=0$	$z=2$	$z=6$	$z=12$
1.0	0.707066	0.689037	0.673304	0.65581	1.03478	1.00101	0.98820	0.97452
2.0	1.24303	1.22092	1.20126	1.17904	2.06029	2.02512	2.00634	1.98521
3.0	1.51862	1.49465	1.47331	1.44912	2.78229	2.74631	2.72424	2.70033

to Coulomb interparticle interactions $\{\mathcal{M}(x_0|0) - \{\mathcal{M}(x_0|z)\}\{\mathcal{M}(x_0|0)\}^{-1}$ at $z = 2$ equals 2.5% at $x_0 = 1$ and 1.6% at $x_0 = 3$; at $z = 6$ respectively 4.8% at $x_0 = 1$ and 3% at $x_0 = 3$; similarly at $z = 12$ we have 7.2% at $x_0 = 1$ and 4.6% at $x_0 = 3$. The relative decrease of the radius due to Coulomb interparticle interactions is a monotonously decreasing function of the relativistic parameter x_0 and a monotonously increasing function of the charge z and does not exceed 5.8%.

Equation (61) can be simplified by taking into account that derivatives $d\mathcal{E}_{\rm cor}(x)/dx$ and $d\mathcal{E}_2(x)/dx$ almost do not depend on x. Therefore, $\varphi_2(x|z)$ is very small and it can neglected. The function $\varphi_1(x|z)$ weakly depends on x and can be approximated by expression $\varphi_1(x|z) \approx \beta(z)\varphi_1(x_0|z)$,

$$\varphi_1(x_0|z) = \alpha_0\left[\frac{1}{\pi} + \frac{2d_0}{3\gamma}z^{2/3}\right] + \frac{4}{3}\alpha_0^2\left\{\frac{d\varepsilon_{\rm cor}(x_0)}{dx_0} + z^{4/3}\frac{d\varepsilon_2(x_0)}{dx_0}\right\}. \tag{65}$$

Since for small and intermediate values of the variable ξ

$$\left\{\tilde{y}^2(\xi|z) + \frac{2}{\varepsilon_0}\tilde{y}(\xi|z)\right\}^{1/2} \approx \tilde{y}(\xi|z)\left\{1 + \frac{2}{\varepsilon_0}\right\}^{1/2}, \tag{66}$$

equation (61) can be approximately rewritten in the form

$$\left\{1 - \left(1 + \frac{2}{\varepsilon_0}\right)^{1/2}\beta(z)\varphi_1(x_0|z)\right\}\Delta_\xi\tilde{y}(\xi|z) = -\left\{\tilde{y}^2(\xi|z) + \frac{2}{\varepsilon_0}\tilde{y}(\xi|z)\right\}^{3/2}. \tag{67}$$

Passing from the variable ξ to the variable ζ employing $\xi = k\zeta$ at

$$k \equiv k(x_0|z) = \left\{1 - \left(1 + \frac{2}{\varepsilon_0}\right)^{1/2} \beta(z)\varphi_1(x_0|z)\right\}^{1/2}, \tag{68}$$

equation (67) acquires the form

$$\Delta_\zeta \tilde{y}(k\zeta|z) = -\left\{\tilde{y}^2(k\zeta|z) + \frac{2}{\varepsilon_0}\tilde{y}(k\zeta|z)\right\}^{3/2}. \tag{69}$$

Due to the fact that equation (69) does not differ from equation (17), $\tilde{y}(k\zeta|z) = y(\zeta)$, where $y(\zeta)$ is the solution of equation (17). From the condition $y(\zeta) = 0$ we obtain the dimensionless radius of a star $\zeta_1(x_0) = \xi_1(x_0)$, and from the condition $\tilde{y}(\xi|z) = 0$ – the radius $\xi_1(x_0|z) = k\xi_1(x_0)$. The mass and radius of a white dwarf are determined by the equilibrium equation in approximation (67)

$$\begin{aligned} M(x_0|\mu_e|z) &= k^3(x_0|z)\frac{M_0}{\mu_e^2}\mathcal{M}(x_0), \\ R(x_0|\mu_e|z) &= k(x_0|z)\frac{R_0\xi_1(x_0)}{\mu_e\varepsilon_0(x_0)}, \end{aligned} \tag{70}$$

where $\mathcal{M}(x_0)$ and $\xi_1(x_0)$ correspond to the Chandrasekhar model. Approximations (65) and (66) create small errors in the calculation of the model characteristics. At $\beta(z) = 0.75 + (z-6)\cdot 0.0033$ the relative deviation of mass, calculated by formula (70) from the above in Tab. 2, is less than 0.1%.

Approximations (65) and (66) allow us to rewrite the equilibrium equation of a white dwarf taking into account the axial rotation and Coulomb interparticle interactions

$$\left\{1 - \left(1 + \frac{2}{\varepsilon_0}\right)^{1/2} \beta(z)\varphi_1(x_0|z)\right\}\Delta_{\xi,\theta}\tilde{Y}(\xi,\theta) = \Omega^2 - \left\{\tilde{Y}^2(\xi,\theta) + \frac{2}{\varepsilon_0}\tilde{Y}(\xi,\theta)\right\}^{3/2}. \tag{71}$$

By substitution $\xi = k(x_0|z)\zeta$, equation (71) reduces to equation (10) for the function $\tilde{Y}(k\zeta,\theta)$. Therefore, $\tilde{Y}(k\zeta,\theta) = Y(\zeta,\theta)$ is the solution of equation (10) in which there should be made the replacement $\xi \to \zeta$. Thus, all the characteristics of a white dwarf are obtained from those calculated by formulae (37)-(49). Since $\mathbf{r} = k(x_0|z)\lambda(x_0)\boldsymbol{\xi}$, then

$$\begin{aligned} &\xi_e(x_0|\omega|z) = k(x_0|z)\xi_e(x_0|\omega); \;\; \xi_p(x_0|\omega|z) = k(x_0|z)\xi_p(x_0|\omega); \\ &v(x_0|\omega|z) = k^3(x_0|z)v(x_0|\omega); \;\; \mathcal{M}(x_0|\omega|z) = k^3(x_0|z)\mathcal{M}(x_0|\omega); \\ &\mathcal{J}(x_0|\omega|z) = k^5(x_0|z)\mathcal{J}(x_0|\omega); \;\; |\mathscr{E}(x_0|\omega|z)| = k^5(x_0|z)|\mathscr{E}(x_0|\omega)|; \\ &g_e(x_0|\omega|z) = k(x_0|z)g_e(x_0|\omega). \end{aligned} \tag{72}$$

Table 3. Macroscopic characteristics of the white dwarf V1460 Her with a known mass.

z	$\mathcal{M}(x_0\|\omega)$	$M/M_\odot$	$\xi_p(x_0\|\omega\|z)$	R_p, 10^3km	$\xi_e(x_0\|\omega\|z)$	R_e, 10^3km
2	1.20668	0.869	1.8898	6.66	1.9774	6.96
6	1.20668	0.869	1.8810	6.62	1.9672	6.93
12	1.20668	0.869	1.8685	6.58	1.9551	6.89

Table 4. Macroscopic characteristics of the white dwarf LAMOST J024048.51+195226.9.

z	$\mathcal{M}(x_0\|\omega\|z)$	$M/M_\odot$	$\xi_p(x_0\|\omega\|z)$	R_p, 10^3km	$\xi_e(x_0\|\omega\|z)$	R_e, 10^3km
2	1.0568	0.763	1.3638	7.50	1.9289	10.60
6	1.0378	0.749	1.3556	7.45	1.9173	10.54
12	1.0155	0.733	1.3458	7.40	1.9034	10.46

Table 5. Macroscopic characteristics of the white dwarf CTCV J2056-3014.

z	$\mathcal{M}(x_0\|\omega\|z)$	$M/M_\odot$	$\xi_p(x_0\|\omega\|z)$	R_p, 10^3km	$\xi_e(x_0\|\omega\|z)$	R_e, 10^3km
2	0.9450	0.682	1.1826	8.07	1.7142	11.70
6	0.9266	0.669	1.1749	8.02	1.7030	11.63
12	0.9049	0.653	1.1656	7.96	1.6896	11.54

5. Conclusions

It is known from observations that the average masses of single white dwarfs are close to $0.6M_\odot$. There is a small number of white dwarfs of large masses in binary systems, which are close to the Chandrasekhar limit due to accretion effects. The considered objects in this article should belong to the typical moderately massive white dwarfs, the prototype of which is Sirius B. From numerous observations it follows that the mass of Sirius B equals $(1.018 \pm 0.0011)M_\odot$, and its average radius is $(0.8089 \pm 0.0046) \cdot 10^{-2} R_\odot \simeq (5.63896 \cdot 10^3 \pm 32.03164)$ km (Bond et al., 2017). Obviously, not very large masses of such white dwarfs are due to their rapid rotation. Unfortunately, there is no reliable data on the angular velocity of Sirius B.

1. For the white dwarf V1460 Her from the observations there are known the dynamic mass and angular velocity, which creates an ideal possibility to determine the relativistic parameter x_0 and calculation of all required characteristics. Axial rotation and Coulomb interparticle interactions are competing factors, their impacts being small. Therefore, we take them into account in a linear approximation, neglecting the cross-effects and use of the relativistic parameter x_0, which were found within the model with axial rotation (without Coulomb interparticle interactions). As it was shown in Tab. 3, the influence of Coulomb interparticle interactions lead to decreasing of white dwarf sizes.

2. From observations of white dwarfs LAMOST J024048.51+195226.9 and CTCV J2056-3014 there are known only their angular velocities. In this case, we performed an evaluation of characteristics (mass, polar and equatorial radii), assuming that the observed angular velocity is close to the maximal angular velocity $\omega_{\max}$. Dependence of characteristics on a chemical composition parameter (on average the nuclear charge z) for given two white dwarfs is illustrated in Tabs. 4 and 5. Coulomb interparticle interactions lead to decreasing of the mass and sizes of white dwarfs without changing a mass-radius relation.

3. As it follows from our calculations, the values of masses of three white dwarfs are close to each other and do not exceed the mass of the Sun. Moments of inertia of these white dwarfs have the same order of magnitude, and in the Chandrasekhar model they equal 0.63670 for V1460 Her, 0.76149 for LAMOST J024048.51+195226.9 and 0.80515 for CTCV J2056-3014. To calculate the moment of inertia of the white dwarf Sirius B in the Chandrasekhar model, it is necessary to solve the inverse problem, determining parameters x_0 and μ_e from the system of equations

$$\begin{aligned} R(x_0|\mu_e) &= \frac{R_0}{\mu_e \varepsilon_0}\xi_1(x_0),\ M(x_0|\mu_e) = \frac{M_0}{\mu_e^2}\mathcal{M}(x_0), \\ \mathcal{M}(x_0) &= \int\limits_0^{\xi_1(x_0)} \left\{ y^2(\xi) + \frac{2}{\varepsilon_0} y(\xi) \right\}^{3/2} \xi^2 d\xi, \end{aligned} \tag{73}$$

putting instead $R(x_0|\mu_e)$ and $M(x_0|\mu_e)$ their observed data. Thus we find that $x_0 = 2.3806$, $\mu_e = 1.9879$, and the dimensionless moment of inertia calculated by the formula

$$\mathcal{J}(x_0|0) = \frac{2}{3\varepsilon_0^2} \int\limits_0^{\xi_1(x_0)} \left\{ y^2(\xi) + \frac{2}{\varepsilon_0} y(\xi) \right\}^{3/2} \xi^4 d\xi \tag{74}$$

equals 0.51178. All this gives reasons to hope that the white dwarf Sirius B has a rapid axial rotation, and determining its speed from observations is an urgent problem.

References

Ashley, R. P., Marsh, T. R., Breedt, E., et al., V1460 Her: a fast spinning white dwarf accreting from an evolved donor star. 2020, *Monthly Notices of the Royal Astronomical Society*, **499**, 149, DOI: 10.1093/mnras/staa2676

Bond, H. E., Schaefer, G. H., Gilliland, R. L., et al., The Sirius System and Its Astrophysical Puzzles: Hubble Space Telescope and Ground-based As-

trometry. 2017, *The Astrophysical Journal*, **840**, 70, DOI: 10.3847/1538-4357/aa6af8

Carr, W. J., Energy, Specific Heat, and Magnetic Properties of the Low-Density Electron Gas. 1961, *Phys. Rev.*, **122**, 1437, DOI: 10.1103/PhysRev.122.1437

Chandrasekhar, S., The Maximum Mass of Ideal White Dwarfs. 1931, *Astrophysical Journal*, **74**, 81, DOI: 10.1086/143324

Chandrasekhar, S., The equilibrium of distorted polytropes. I. The rotational problem. 1933, *Monthly Notices of the RAS*, **93**, 390, DOI: 10.1093/mnras/93.5.390

Fuchs, K., A Quantum Mechanical Investigation of the Cohesive Forces of Metallic Copper. 1935, *Proceedings of the Royal Society of London. Series A, Mathematical and Physical Sciences*, **151**, 585

James, R. A., The Structure and Stability of Rotating Gas Masses. 1964, *Astrophysical Journal*, **140**, 552, DOI: 10.1086/147949

Lopes de Oliveira, R., Bruch, A., Rodrigues, C. V., Oliveira, A. S., & Mukai, K., CTCV J2056-3014: An X-Ray-faint Intermediate Polar Harboring an Extremely Fast-spinning White Dwarf. 2020, *The Astrophysical Journal*, **898**, L40, DOI: 10.3847/2041-8213/aba618

Milne, E. A., The equilibrium of a rotating star. 1923, *Monthly Notices of the RAS*, **83**, 118, DOI: 10.1093/mnras/83.3.118

Pelisoli, I., Marsh, T. R., Dhillon, V. S., et al., Found: a rapidly spinning white dwarf in LAMOST J024048.51+195226.9. 2021, *Monthly Notices of the Royal Astronomical Society: Letters*, **509**, L31, DOI: 10.1093/mnrasl/slab116

Pines, D. & Noziéres, P. 1966, *The Theory of Quantum Liquids: Normal Fermi Liquids*

Roxburgh, I. W., On Models of Non Spherical Stars. II. Rotating White Dwarfs. With 2 Figures in the Text. 1965, *Zeitschrift fuer Astrophysik*, **62**, 134

Salpeter, E. E., Energy and Pressure of a Zero-Temperature Plasma. 1961, *Astrophysical Journal*, **134**, 669, DOI: 10.1086/147194

Tassoul, J. L. 1978, *Theory of rotating stars*

Vavrukh, M., Dzikovskyi, D., & Smerechynskyi, S., White dwarfs with rapid rotation. 2022, *Mathematical Modeling and Computing*, **9**, 278, DOI: 10.23939/mmc2022.02.278

Vavrukh, M. V., Dzikovskyi, D. V., & Smerechynskyi, S. V., The influence of the interactions on the degenerate dwarfs characteristics. 2018, *Journal of Physical Studies*, **22**, 1901, DOI: 10.30970/jps.22.1901

Contrib. Astron. Obs. Skalnaté Pleso **52/2**, 44 – 57, (2022)
https://doi.org/10.31577/caosp.2022.52.2.44

Photometric observations of six Mars-crossing asteroids with the 1-m INASAN telescope at Mt. Koshka

A.S. Kravtsova[1,2], S. I. Barabanov[2] and I.M. Volkov[1,2]

[1] *Sternberg Astronomical Institute, Lomonosov Moscow State University, Universitetskij Ave. 13, 119992 Moscow, Russia (E-mail: kravts@yandex.ru,hwp@yandex.ru)*

[2] *Institute of Astronomy of the Russian Academy of Sciences, 48 Pyatnitskaya street, 119017 Moscow, Russia (E-mail: sbarabanov64@yandex.ru)*

Received: June 24, 2022; Accepted: October 6, 2022

Abstract. We present observations of six asteroids crossing the orbit of Mars obtained at Mt. Koshka observatory of INASAN in 2014–2016. Our multicolor photometry made it possible to determine the apparent magnitudes of asteroids in *BVRcIc* photometric bands, as well as their taxonomic class according to Tholen's classification. The periods of rotation were determined for asteroids 9773, 32575, 97679, and 313591. For asteroid 8355 Masuo the rotation period determined earlier was confirmed. Our observations support the long period of rotation for asteroid 122463 (presumably about 19 days).

Key words: asteroids: photometry – asteroids: Tholen classification

1. Introduction

Since 2010, multicolor observations of asteroids have been carried out at the 1-m telescope in Simeiz. The most important asteroids are those approaching the Earth's orbit (NEA). However, not a lot of NEA have a sufficient brightness to obtain high-quality multicolor photometric observations. So we choose objects from much more numerous Mars-crossing asteroids which are related to the NEA group. These asteroids in some cases can cross the Earth's orbit or approach the Earth. NEA and Mars-crossing asteroids can move from one group to another due to orbit changing. It is important to investigate the taxonomy and rotation of Mars-crossing asteroids, compare them to NEA and follow the evolution of their orbits.

Mars-crossing asteroids are also interesting because of their connection to Mars. Automatic vehicles are visiting Mars' orbit and go down to its surface. Small objects associated with Mars, such as meteor showers and fireballs, can seriously interfere with the work of automatic stations exploring its surface and, in the future, inhabited settlements. We must have comprehensive information

about the physical and mineralogical properties of near-Martian asteroids. Some of them can be in future a source of industrial minerals.

2. Observations

Thoroughly calibrated photometric systems make it possible to obtain reliable data on the physical and mineralogical features of the small bodies in Solar System.

Our photometrical multicolor observations were carried out with a Zeiss-1000 cassegrain (D =1 m, $f/12.7$) in the Simeiz observatory of INASAN. An FLI PL-09000 (3056x3056) CCD array was equipped with a $BVRcIc$ filter set which realized the Johnson-Cousins photometric system. 5x5 binning provided a 0.97" pixel size. Seeing was usually 3-4". More information about the observatory and telescope one may find in Nikolenko et al. (2019).

Table 1 presents the orbital parameters of asteroids under investigation from the Small Body Database[1].

Table 2 contains their physical parameters from the same source.

Table 1. Elements of the orbits. The columns sequentially list: The object number, the size of the semi-major axis of the orbit a, its eccentricity e, its inclination to the line of sight i, the longitude of the ascending node W, the argument of perihelion w, the Earth Minimum Orbit Intersection Distance (MOID), the Jupiter MOID, and the Jupiter Tisserand invariant Tj.

Object	a	e	i	W	w	Earth MOID	Jupiter MOID	Tj
	au		deg	deg	deg	au	au	
8355	2.336	0.288	7.705	154.140	196.326	0.657	2.425	3.499
9773	2.681	0.388	14.700	277.512	15.582	0.628	1.507	3.221
32575	2.225	0.337	2.232	229.088	98.305	0.465	2.395	3.569
97679	1.571	0.132	50.815	196.325	138.410	0.403	3.539	4.001
122463	2.162	0.321	8.716	157.614	158.169	0.458	2.478	3.613
313591	2.382	0.423	11.885	312.090	32.101	0.382	2.086	3.384

Information about the observations is presented in Table 3.

The details of our observations' method and analysis technique are described in Volkov et al. (2019) and Barabanov et al. (2019). The transformation coefficients from the instrumental system to the standard one were published in Barabanov et al. (2021b). Some previous results on asteroids 8355, 9773, and 32575 were published in Barabanov et al. (2021a). For taxonomy derivation, a

[1]https://ssd.jpl.nasa.gov/tools/sbdb_lookup.html

Table 2. Physical parameters. The columns sequentially list: The object number, the absolute stellar magnitude, its diameter D, the geometric albedo and the rotation period P.

Object	Absolute mag	D, km	Albedo	P, hours
8355	14.40	3.874	0.277	6.0677
9773	13.79	4.016	0.377	2.74595
32575	15.42	2.157	0.325	4.5344
97679	16.64	-	-	-
122463	15.59	-	-	426
313591	16.56	-	-	-

Table 3. Observation log. The columns sequentially list: The object, the observation date, the heliocentric distance r, the geocentric distance Δ, the phase angle α, exposure times and the number of frames.

Object	Date (JD)	r (au)	Δ (au)	α (deg)	exposure (sec)	Frames
8355	2456918	1.6691	0.6717	7.7	30-120	283
9773	2457242	1.6604	0.6828	15.0	30-60	160
	2457248	1.6687	0.7099	17.7	30-60	314
	2457249	1.6702	0.7149	18.1	30-60	402
	2457250	1.6718	0.7202	18.6	30-60	160
32575	2456881	1.4762	0.4642	6.3	60	160
	2456882	1.4757	0.4634	5.9	60-150	224
97679	2456937	1.3951	0.4074	12.7	20-60	649
	2456939	1.3972	0.4076	11.5	30-60	745
	2456940	1.3983	0.4087	11.3	30-40	503
	2456942	1.4005	0.4127	11.8	20-60	593
122463	2457611	1.4686	0.4593	7.1	60-80	57
	2457612	1.4687	0.4597	7.2	60-80	112
	2457613	1.4690	0.4603	7.3	60-80	83
313591	2456884	1.3830	0.4289	26.1	120-180	96
	2456885	1.3819	0.4263	25.8	120-180	104
	2456886	1.3810	0.4238	25.5	120-180	136

set of standard spectra of taxonomic classes were used, see Tholen (1989) and Tholen (1984).

3. Processing of observations.

Our multicolor observations made it possible to determine with sufficient accuracy the apparent stellar magnitudes and color indices of asteroids - see Table 4. The choice of reference stars in each frame satisfies the following conditions: the stars should be sufficiently bright (10^m–12^m), their color indices $B-V<1.2$ and they should be located at the same frame with the asteroid (Barabanov et al. (2021b)). The number of reference stars in a single frame satisfying these conditions varied from 1 to 4. We interpolated tables from Straižys (1992) to find $V-Rc$, $Rc-Ic$ color indices of each reference star according to its $B-V$ color index derived from B, V magnitudes taken from the APASS DR10 catalogue[2].

Magnitudes of asteroid 8355, for technical reasons, were derived with only one reference star. In the case of asteroid 32575, the error obtained from observations seems to be underestimated.

Table 4. Stellar magnitudes of asteroids in $BVRcIc$ and their color indices with errors.

Object	*B*	*V*	*Rc*	*Ic*	*B-V*	*V-Rc*	*V-Ic*
8355	16.29	15.36	14.80	14.41	0.93	0.56	0.95
	0.08	0.15	0.22	0.23	0.09	0.08	0.1
9773	16.01	15.10	14.61	14.25	0.91	0.48	0.85
	0.08	0.15	0.22	0.23	0.09	0.08	0.1
32575	16.06	15.23	14.82	14.46	0.84	0.41	0.77
	0.03	0.02	0.02	0.04	0.05	0.02	0.06
97679	17.22	16.29	15.83	15.50	0.93	0.46	0.79
	0.13	0.12	0.07	0.09	0.06	0.07	0.07
122463	16.11	15.21	14.93	14.33	0.91	0.27	0.88
	0.06	0.02	0.08	0.08	0.07	0.08	0.16
313591	17.28	16.57	16.23	15.90	0.72	0.33	0.66
	0.05	0.05	0.1	0.13	0.04	0.08	0.1

A set of standard spectra of taxonomic classes we construct using Tholen (1984) description. We transferred stellar magnitudes in different spectral ranges to energetic units, normalized them to the flow in the V band and compare with standard Tholen's spectra. The specific class of asteroids was determined by the minimum of the mean-square deviation of the coarse spectrum of the asteroid obtained from observations (four points) from the standard spectrum, as shown in the Figures with even numbers below.

Next, we present for each asteroid the relative spectrum energy distribution and phased with rotational period light curves Table 5.

[2]https://www.aavso.org/apass

3.1. (8355) Masuo 1989 RQ1

(8355) Masuo 1989 RQ1 was discovered on September 5, 1989 at the Palomar Observatory by the American astronomer Eleanor Helin and named after Japanese astronomer Masuo Tanaka (University of Tokyo).

Our observations of this asteroid were carried out only for 5 hours, which makes it impossible to correct its period 6.0677 h – from Small Body Database[3]. We can only say that our observations do not contradict previous data, see Fig. 1. Estimates of the variability semi-amplitude in different spectral regions are: $A_B = 0.^m09, A_V = 0.^m1, A_{Rc} = 0.^m1, A_{Ic} = 0.^m09$. The distribution of energy in the spectrum best corresponds to the taxonomic class A - see Fig. 2. There is a relatively large mismatch in B due to its big error.

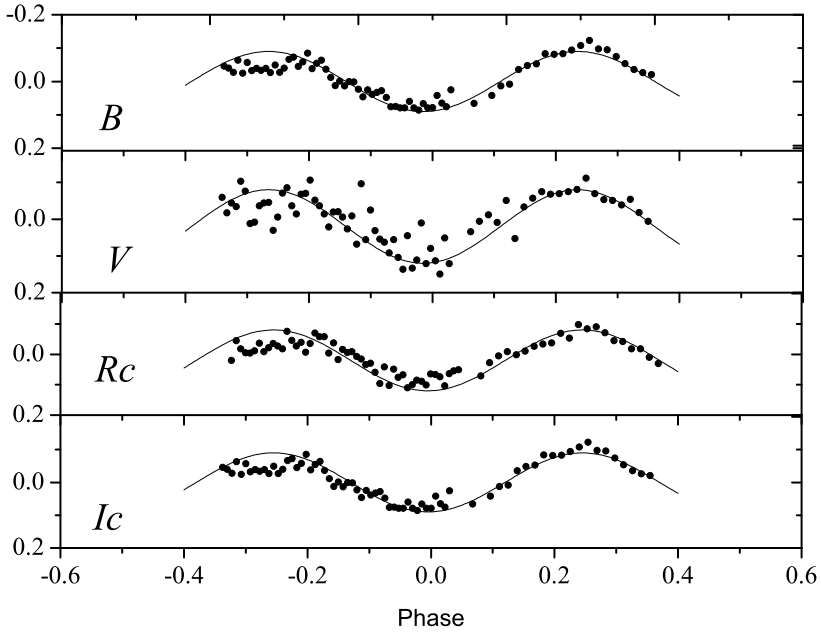

Figure 1. The phased light curve of 8355 asteroid in $BVRcIc$ bands. $P = 6.0677$ h. $B_{mean} = 16^m.29$, $V_{mean} = 15^m.36$, $Rc_{mean} = 14^m.80$, $Ic_{mean} = 14^m.41$. The solid curve corresponds to a sinusoid with a variability amplitude.

[3]https://ssd.jpl.nasa.gov/tools/sbdb_lookup.html

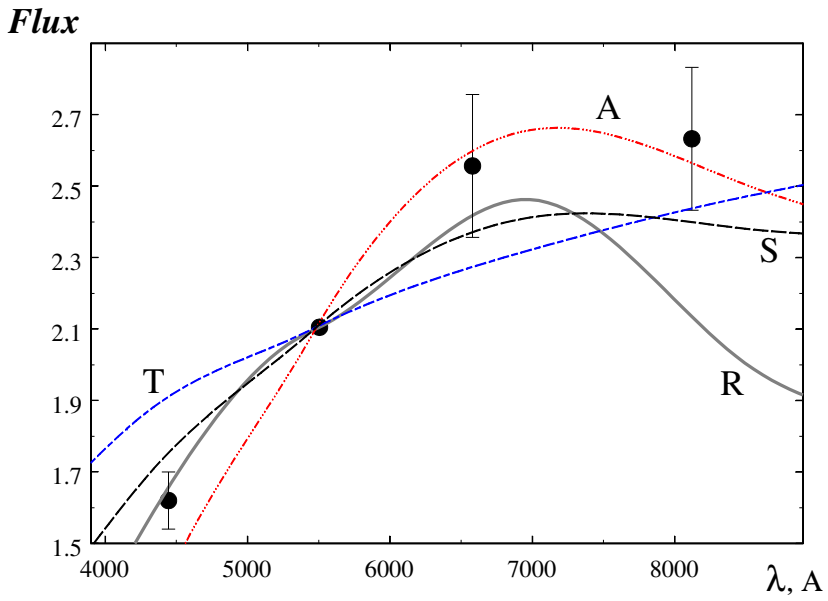

Figure 2. Energy distribution in the spectrum of asteroid 8355 Masuo. Dimensionless quantities are plotted along the y axis - the flux normalized to the solar one with a coefficient according to the works of Tholen. The curves of different colors correspond to some of the indicated standard taxonomic classes according to Tholen (1989), Tholen (1984). Black circles with error bars are observed data. Everything is normalized to the flux in the V filter, so that this point is considered accurate (indicated without an error bar), and the inaccuracy of observations in V is taken into account in the flux errors in other spectral bands.

3.2. (9773) 1993 MG1

(9773) 1993 MG1 was discovered on June 23, 1993 at the Palomar Observatory by astronomer Eleanor Helin (E.F. Helin).

We have determined the value of the rotation period $P = 2.7461 \pm 0.0002$ hours - see Fig. 3, which confirms the value determined by Benishek & Brincat (2016) within their errors. We can't get better accuracy due to the short duration of our observations. Estimates of the variability semi-amplitude in different spectral regions are: $A_B = 0.^m11$, $A_V = 0.^m13$, $A_{Rc} = 0.^m13$, $A_{Ic} = 0.^m14$. The taxonomic class corresponds to the class S - see Fig. 4.

3.3. (32575) 2001 QY78

(32575) 2001 QY78 was discovered on August 16, 2001 as part of the LINEAR (Lincoln Near-Earth Asteroid Research) program at the Socorro Observatory,

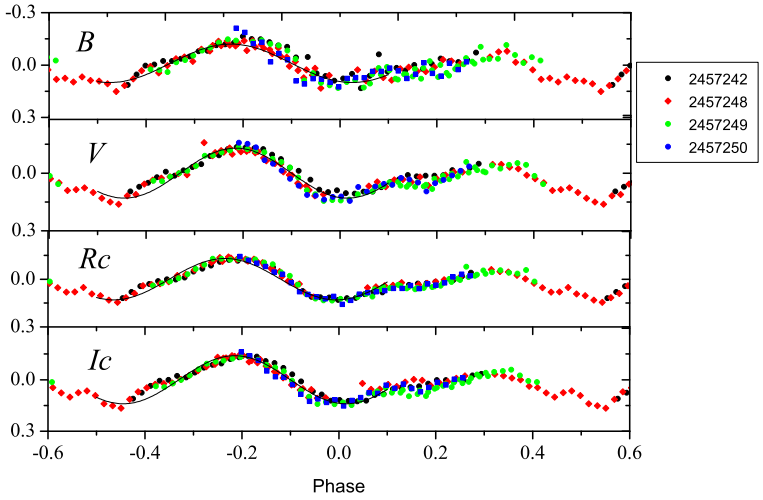

Figure 3. The phased light curve of 9773 asteroid in $BVRcIc$ bands. $P = 2.74608$ h. $B_{mean} = 16^m.01$, $V_{mean} = 15^m.10$, $Rc_{mean} = 14^m.61$, $Ic_{mean} = 14^m.25$. Points of the same color correspond to one observation night: The legend shows correspondence between color and observation JD. The solid curve corresponds to a sinusoid with a variability amplitude.

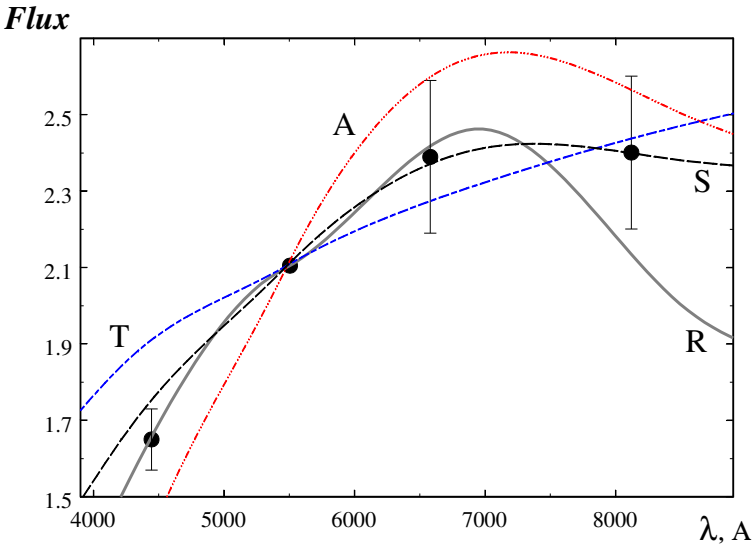

Figure 4. Energy distribution in the spectrum of asteroid 9773. Symbols are the same as in Fig. 2.

New Mexico.

The rotation period of the asteroid was determined by us as $P = 4.5331 \pm 0.0017$ hours, which coincides with previous measurements (4.5344 h – see the Small Body Database[4]) within errors. As in the case of asteroid 9733, increasing the duration of observations will improve the accuracy of the value of the rotation period. The phased light curve corresponding to the found period is shown in Fig. 5. Estimates of the variability semi-amplitude in different spectral regions are: $A_B = 0.^m41, A_V = 0.^m4, A_{Rc} = 0.^m4, A_{Ic} = 0.^m38$. From $BVRcIc$ photometry, the value of the taxonomic class Q is obtained, see Fig. 6.

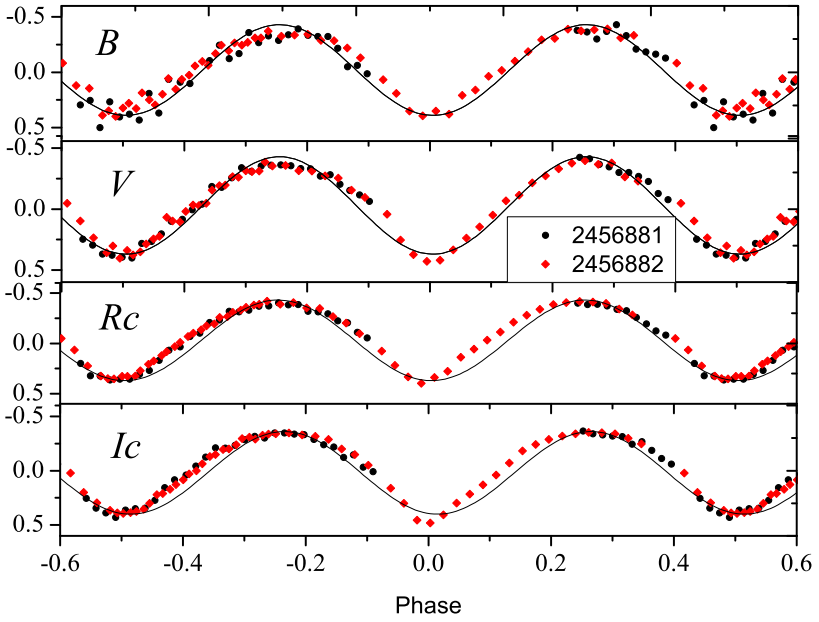

Figure 5. The phased light curve of 32575 asteroid in $BVRcIc$ bands. $P = 4.53312$ h. $B_{mean} = 16^m.06$, $V_{mean} = 15^m.23$, $Rc_{mean} = 14^m.82$, $Ic_{mean} = 14^m.46$. Points of the same color correspond to one observation night: The legend shows correspondence between color and observation JD. The solid curve corresponds to a sinusoid with a variability amplitude.

3.4. (313591) 2003 MB7

(313591) 2003 MB7 was discovered on June 28, 2003 as part of the LINEAR program at the Socorro Observatory, New Mexico.

[4]https://ssd.jpl.nasa.gov/tools/sbdb_lookup.html

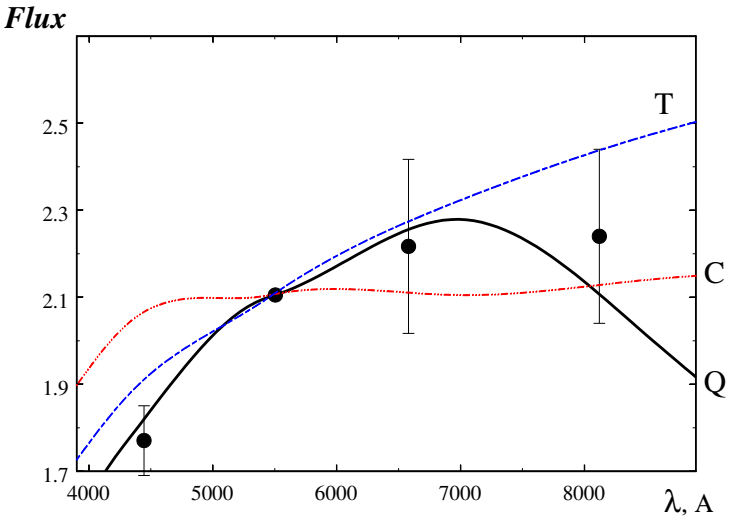

Figure 6. Energy distribution in the spectrum of asteroid 32575. Symbols are the same as in Fig. 2.

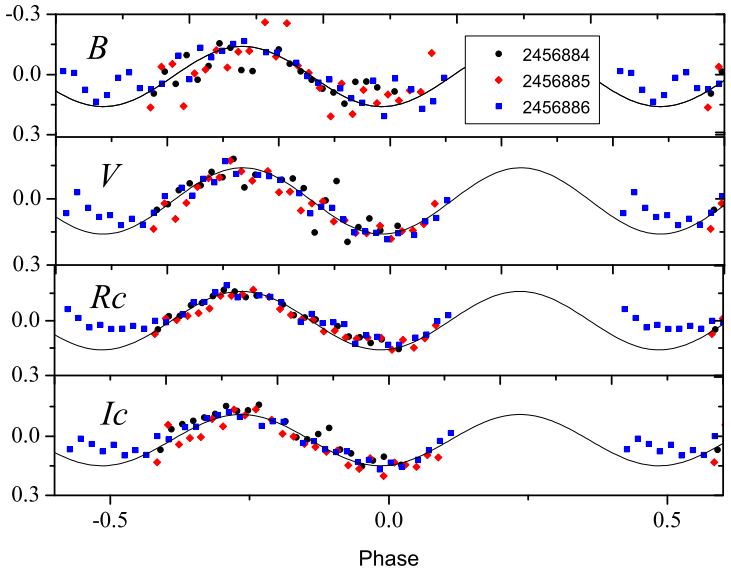

Figure 7. The phased light curve of 313591 asteroid in $BVRcIc$ bands. $P = 7.92$ h. $B_{mean} = 17^m.28$, $V_{mean} = 16^m.57$, $Rc_{mean} = 16^m.23$, $Ic_{mean} = 15^m.90$. Points of the same color correspond to one observation night: The legend shows correspondence between color and observation JD. The solid curve corresponds to a sinusoid with a variability amplitude.

We estimated the value of the period $P \approx 7.92$ hours, see Fig. 7. The periodogram built with our program (Volkov, 2022) shows two approximately equal peaks at the given period value and at 6.85 hours. After close examination of phased with these periods light curves, we have chosen the larger one as it has less systematic deviations. It is impossible to determine the precise value of the period from the available data. The final conclusion can be made only after additional observations. Estimates of the variability semi-amplitude in different spectral regions are: $A_B = 0.^m15, A_V = 0.^m15, A_{Rc} = 0.^m16, A_{Ic} = 0.^m14$. Very accurate values of the color indices of the asteroid have been obtained, they correspond to Tholen's taxonomic class C, see Fig. 8.

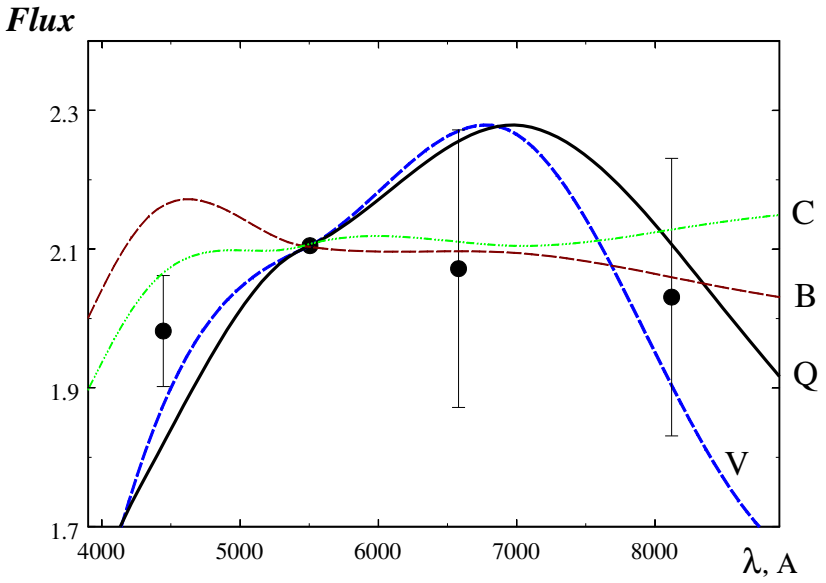

Figure 8. Energy distribution in the spectrum of asteroid 313591. Symbols are the same as in Fig. 2.

3.5. (97679) 2000 GG2

(97679) 2000 GG2 was discovered on April 3, 2000 as part of the LINEAR program at the Socorro Observatory, New Mexico. At the time of processing the observations, no physical and chemical parameters were known, except for the absolute magnitude, see Table 2. We have succeeded in detecting periodic variations in brightness, but the accuracy of observations is comparable to the amplitude of the variations, which can lead to an erroneous value of the rotation period, see Fig. 9. We consider this period to be 7.964 ± 0.004 hours. Further

observations will help to confirm this value. Estimates of the variability semi-amplitude in different spectral regions are: $A_B = 0.^m15, A_V = 0.^m15, A_{Rc} = 0.^m08, A_{Ic} = 0.^m12$.

Multicolor observations have allowed us to determine the taxonomic class of this asteroid as S, although there is a non-zero probability that it can also belong to the R class – see Fig. 10.

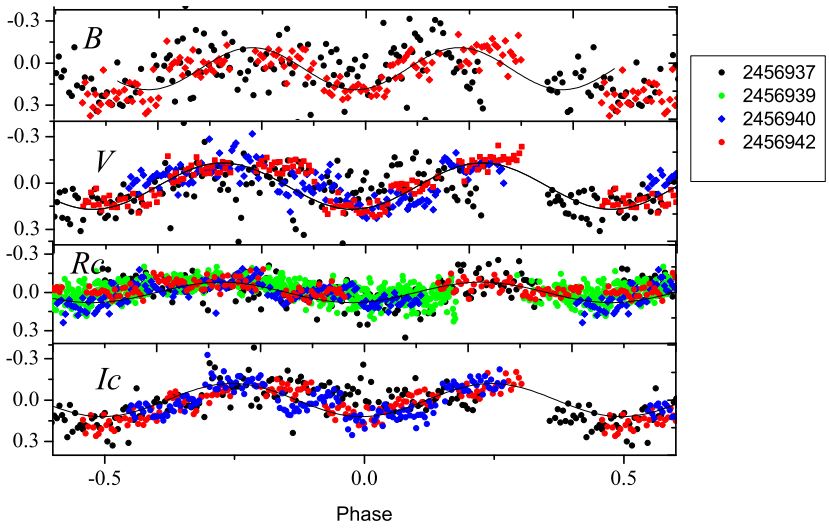

Figure 9. The phased light curve of 97679 asteroid in $BVRcIc$ bands. $P = 7.9644$ h. $B_{mean} = 17^m.22$, $V_{mean} = 16^m.29$, $Rc_{mean} = 15^m.83$, $Ic_{mean} = 15^m.50$. Points of the same color correspond to one observation night: The legend shows correspondence between color and observation JD. The solid curve corresponds to a sinusoid with a variability amplitude.

3.6. (122463) 2000 QP148

(122463) 2000 QP148 was discovered as part of the LINEAR program at the Socorro Observatory, New Mexico. The estimated value of the rotation period is 426.3 hours, i.e. more than 17 days, see Table 2, and examples of asteroid light curves[5]. With only three consecutive nights of observations at hand, we can neither confirm nor deny this value. Our observations are presented in Fig. 11. We did not find any brightness' fluctuations at times from tens of minutes to several hours. To accurately determine the rotation period, it is necessary to organize systematic observations of this object during several months. The distribution of energy in the spectrum is shown in Fig. 12. We believe that the Tholen taxonomic class of this asteroid corresponds to the T class.

[5]https://www.asu.cas.cz/ asteroid/122463.png

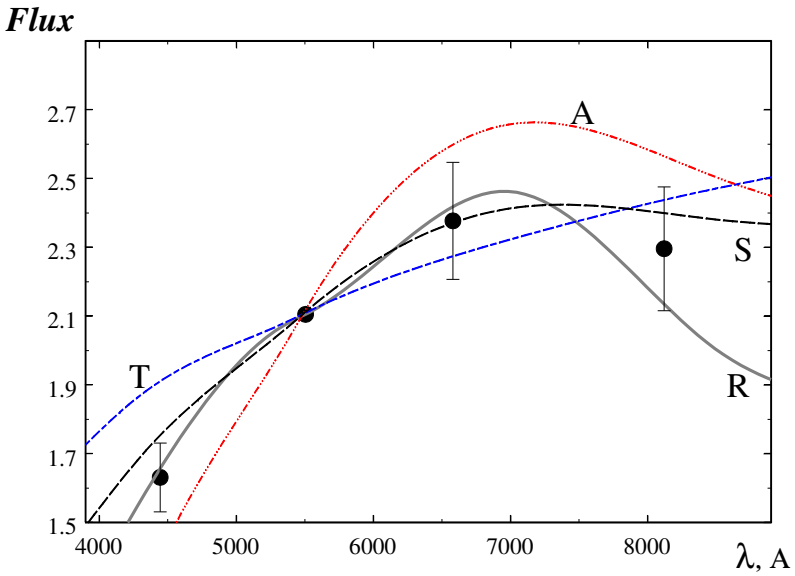

Figure 10. Energy distribution in the spectrum of asteroid 97679. Symbols are the same as in Fig. 2.

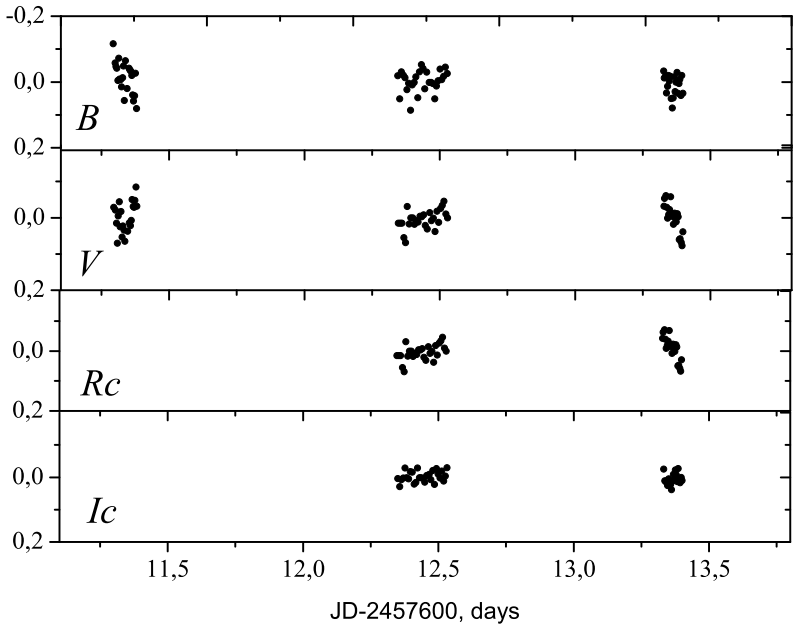

Figure 11. The non-phased light curve of 122463 asteroid in $BVRcIc$ bands. $B_{mean} = 16^m.11$, $V_{mean} = 15^m.21$, $Rc_{mean} = 14^m.93$, $Ic_{mean} = 14^m.33$.

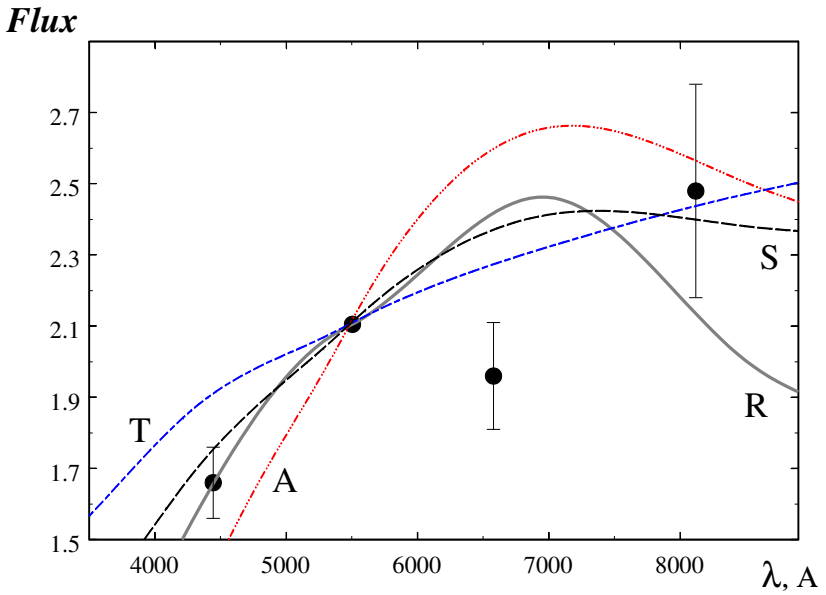

Figure 12. Energy distribution in the spectrum of asteroid 122463. Symbols are the same as in Fig. 2.

Table 5. The rotation period P, the magnitude in the V band (with error), and the Tholen taxonomy.

Object	P, hours	V (err), mag	Taxonomy according Tholen
8355	-	15.36 (15)	A
9773	2.74608 (24)	15.10 (15)	S
32575	4.53312 (17)	15.23 (2)	Q
97679	7.9644 (36)	16.29 (12)	S
122463	-	15.21 (2)	T
313591	7.92 (2)	16.57 (5)	C

4. Conclusion

Photometric multicolor high-precision observations of six Mars-crossing asteroids were made with the Zeiss-1000 telescope in Simeiz during 2014–2016. For all of them, apparent stellar magnitudes and color indices were obtained, and an assessment of the taxonomic class according to Tholen was made. For asteroids 97679 and 313591 the period of proper rotation was estimated for the first time. For asteroids 9773 and 32575 our independent determination of the rotation pe-

riod coincides with the previous estimates within their errors. Asteroid 122463 requires a long (several months) monitoring to determine the value of the rotation period. Undoubtedly, targeted photometric observations of Mars-crossing asteroids will make it possible to determine their origin. These observations will have not only scientific but also obvious practical value.

Acknowledgements. This work has been supported by SAIA scholarship (ASK, IMV).

References

Barabanov, S. I., Kravtsova, A. S., Volkov, I. M., & Bakanas, E. S., Observations of Mars-crossing asteroids with 1-m telescope of Simeiz Observatory of INASAN. 2021a, *INASAN Science Reports*, **6**, 88, DOI: 10.51194/INASAN.2021.6.3.005

Barabanov, S. I., Potanin, S. A., Savvin, A. D., et al., Focus reducer for the Zeiss-1000 telescope of the Simeiz group Zvenigorod Observatory INASAN. 2021b, *INASAN Science Reports*, **6**, 92, DOI: 10.51194/INASAN.2021.6.3.006

Barabanov, S. I., Volkov, I. M., Kravtsova, A. S., Nikolenko, I. V., & Kryuchkov, S. V., Photometric investigations of NEA in Institute of Astronomy of the RAS in 2008-2010. 2019, *INASAN Science Reports*, **4**, 278, DOI: 10.26087/INASAN.2019.4.2.042

Benishek, V. & Brincat, S. M., Rotation Period Determination for (9773) 1993 MG1. 2016, *Minor Planet Bulletin*, **43**, 90

Nikolenko, I. V., Kryuchkov, S. V., Barabanov, S. I., & Volkov, I. M., Telescopes of the INASAN Simeiz Observatory: current state and prospects. 2019, *INASAN Science Reports*, **4**, 85, DOI: 10.26087/INASAN.2019.4.2.015

Straižys, V. 1992, *Multicolor stellar photometry*

Tholen, D. J. 1984, Asteroid Taxonomy from Cluster Analysis of Photometry., PhD thesis, University of Arizona

Tholen, D. J., Asteroid taxonomic classifications. 1989, in *Asteroids II*, ed. R. P. Binzel, T. Gehrels, & M. S. Matthews, 1139–1150

Volkov, I. M., V961 Cep - a new eclipsing variable with δ Sct component. 2022, *Peremennye Zvezdy*, **42**, 1, DOI: 10.24412/2221-0474-2022-42-1-7

Volkov, I. M., Barabanov, S. I., Nikolenko, I. V., Kryuchkov, S. V., & Sergeev, A. V., Spectral observations and photometry of the near-Earth object (25916) 2001 CP44. 2019, *Contributions of the Astronomical Observatory Skalnate Pleso*, **49**, 301

Contrib. Astron. Obs. Skalnaté Pleso **52/2**, 58 – 71, (2022)
https://doi.org/10.31577/caosp.2022.52.2.58

The interaction between hyperons and the surface gravitational redshift of proto neutron star PSR J0740+6620

Xian-Feng Zhao

School of Sciences, Southwest Petroleum University, Chengdu, 610500, China
(E-mail: zhaopioneer.student@sina.com)

Received: August 1, 2022; Accepted: October 8, 2022

Abstract. An effect of the contributions from σ^* and ϕ mesons on the surface gravitational redshift of PNS PSR J0740+6620 is studied with relativistic mean field theory in consideration of a baryon octet. We find that the energy density ε increases relative to the same pressure p as the contributions from σ^* and ϕ mesons are taken into account. Relative to the same central energy density, the radius R of the PNS increases while the mass M, the mass radius ratio M/R and the surface gravitational redshift z of the PNS decrease, taking into account the contributions from σ^* and ϕ mesons. Under the constraint of mass M=2.08 $M_\odot$, considering the contributions from σ^* and ϕ mesons, for the PNS PSR J0740+6620, the radius decreases by about -0.08%, the central energy density increases by about 0.89%, the central pressure increased by about 0.76%, the mass radius ratio increases by about 0.08%, and the surface gravitational redshift increases by about 0.17% from z=0.31663 to z=0.31718.
Key words: stars: binaries - general: stars

1. Introduction

Neutron stars (NSs) are extremely dense because of their large mass M and small radius R (Glendenning, 1997). The mass of an NS will provide constraints on its properties. For example, the mass of an NS would constrain the symmetry energy within it (Li et al., 2021), and perhaps the properties of an NS could also be explained by dark matter (Ding et al., 2022).

Whenever a new massive NS is found, it will inevitably provide some new restrictions on the properties of NS matter. In recent years, several massive NSs have been discovered in succession. In 2010, NS PSR J1614-2230 was observed (Demorest et al., 2010; Fonseca et al., 2016) and three years later another more massive NS PSR J0348+0432 was found (Antoniadis et al., 2013). In 2019, NS PSR J0740+6620 was observed, possibly the most massive NS to date, with a mass of $M = 2.14^{+0.10}_{-0.09}$ $M_\odot$ (2020) (Cromartie et al., 2020), or $M = 2.08^{+0.07}_{-0.07}$ $M_\odot$ (2021) (Fonseca et al., 2021). Why NS PSR J0740+6620 has such a large mass can be explained by scalar tensor theories of gravity by Degollado

et al (Degollado et al., 2020). The mass of NS PSR J0740+6620 suggests that the equation of state (EoS) of NS matter must be hard enough, and it rules out some EoSs that are too soft (Zhou et al., 2019). Since NS PSR J0740+6620 is much more massive than an NS of mass 1.4 $M_\odot$, it is much denser than an NS of mass 1.4 $M_\odot$ (Han et al., 2020).

The mass radius ratio M/R of an NS determines its surface gravitational redshift z. If we know the mass radius ratio M/R of an NS we can calculate its surface gravitational redshift z, and vice versa. NSs are relatively easy to observe. So if we know the surface gravitational redshift z of an NS and the mass of the NS, we can calculate its radius R. It can be seen that the surface gravitational redshift z of an NS is an important physical quantity to describe the properties of an NS (Glendenning, 1997).

An NS is formed from a proto neutron star (PNS) that emit energy through neutrino radiation. The PNS is formed in the center of a supernova explosion due to gravitational collapse. A PNS can have temperatures as high as T=30 MeV. The theoretical study of PNSs is helpful to understand the evolution of NSs (Burrows et al., 1986; Prakash et al., 1997).

The interaction between nucleons in PNS matter can be described in terms of σ, ω and ρ mesons. However, the interaction between the hyperons, which can be described in terms of mesons $f_0(975)$ (denoted as σ^*) and $\phi(1020)$ (denoted as ϕ), must also have some effect on the properties of the PNS matter (Schaffner et al., 1994; Mu et al., 2017).

In this paper, we study the effect of the contributions from σ^* and ϕ mesons on the surface gravitational redshift of the PNS PSR J0740+6620 using the relativistic mean field (RMF) theory (Zhou, 2016).

2. RMF theory of finite temperature NS matter

The Lagrangian density of finite temperature NS matter (Glendenning, 1997; Schaffner et al., 1994) is

$$\begin{aligned}\mathcal{L} = & \sum_B \overline{\Psi}_B(i\gamma_\mu\partial^\mu - m_B + g_{\sigma B}\sigma + g_{\sigma^* B}\sigma^* \\ & -g_{\omega B}\gamma^0\omega - g_{\phi B}\gamma^0\phi - g_{\rho B}\gamma^0\tau_3\rho)\Psi_B \\ & -\frac{1}{2}m_\sigma^2\sigma^2 - \frac{1}{3}g_2\sigma^3 - \frac{1}{4}g_3\sigma^4 \\ & +\frac{1}{2}m_\omega^2\omega^2 + \frac{1}{2}m_\rho^2\rho^2 - \frac{1}{2}m_{\sigma^*}^2\sigma^{*2} + \frac{1}{2}m_\phi^2\phi^2 \\ & + \sum_{\lambda=e,\mu} \overline{\Psi}_\lambda \left(i\gamma_\mu\partial^\mu - m_\lambda\right)\Psi_\lambda. \end{aligned} \quad (1)$$

The energy density and the pressure of mesons and baryons (Glendenning, 1987a,b) are respectively

$$\begin{aligned}\varepsilon &= \frac{1}{2}m_\sigma^2\sigma^2+\frac{1}{2}m_{\sigma^*}^2\sigma^{*2}+\frac{1}{3}g_2\sigma^3+\frac{1}{4}g_3\sigma^4\\ &+\frac{1}{2}m_\omega^2\omega_0^2+\frac{1}{2}m_\phi^2\phi^2+\frac{1}{2}m_\rho^2\rho_{03}^2\\ &+\sum_B\frac{2J_B+1}{2\pi^2}\int_0^\infty\kappa^2 n_B(k)\mathrm{d}\kappa\sqrt{\kappa^2+m_B^{*2}},\end{aligned}\tag{2}$$

$$\begin{aligned}p &= -\frac{1}{2}m_\sigma^2\sigma^2-\frac{1}{2}m_{\sigma^*}^2\sigma^{*2}-\frac{1}{3}g_2\sigma^3-\frac{1}{4}g_3\sigma^4\\ &+\frac{1}{2}m_\omega^2\omega_0^2+\frac{1}{2}m_\phi^2\phi^2+\frac{1}{2}m_\rho^2\rho_{03}^2\\ &+\frac{1}{3}\sum_B\frac{2J_B+1}{2\pi^2}\int_0^\infty\frac{\kappa^4}{\sqrt{\kappa^2+m_B^{*2}}}n_B(k)d\kappa,\end{aligned}\tag{3}$$

where $n_B(k)$ is the Fermi-Dirac distribution function of baryon

$$n_B(k)=\frac{1}{1+exp\left[\left(\varepsilon_B(k)-\mu_B\right)/T\right]}.\tag{4}$$

The energy density and the pressure of leptons are respectively

$$\begin{aligned}\varepsilon &= \sum_l\frac{1}{\pi^2}\int_0^\infty\kappa^2 n_l(k)\mathrm{d}\kappa\sqrt{\kappa^2+m_l^2}\\ &+\sum_\nu\left(\frac{7\pi^2T^4}{120}+\frac{T^2\mu_\nu^2}{4}+\frac{\mu_\nu^4}{8\pi^2}\right),\end{aligned}\tag{5}$$

$$\begin{aligned}p &= \frac{1}{3}\sum_l\frac{1}{\pi^2}\int_0^\infty\frac{\kappa^4}{\sqrt{\kappa^2+m_l^2}}n_l(k)d\kappa\\ &+\sum_\nu\frac{1}{360}\left(7\pi^2T^4+30T^2\mu_\nu^2+\frac{15\mu_\nu^4}{\pi^2}\right).\end{aligned}\tag{6}$$

The mass and radius of the PNS are obtained by the TOV equation (Tolman, 1939; Oppenheimer et al., 1939)

$$\frac{\mathrm{d}p}{\mathrm{d}r}=-\frac{(p+\varepsilon)\left(M+4\pi r^3p\right)}{r\left(r-2M\right)},\tag{7}$$

$$M=4\pi\int_0^R\varepsilon r^2\mathrm{d}r.\tag{8}$$

The PNS's surface gravitational redshift can be obtained by (Glendenning, 1997):

$$z = \frac{1}{\sqrt{1-2(M/R)}} - 1. \tag{9}$$

3. Parameters

In this work, we select eight sets of nucleon coupling parameters to calculate PNSs: DD-ME1 (Typel et al., 1999), GL85 (Glendenning, 1985), GL97 (Glendenning, 1997), TW99 (Typel et al., 1999), GM1 (Glendenning et al., 1991), FSUGold (Todd-Rutel et al., 2005), FSU2R (Laura et al., 2017) and FSU2H (Laura et al., 2017). In the early stage of formation, the temperature of the PNS can be as high as 30 MeV. We choose the PNS PSR J0740+6620's temperature as T=20 MeV (Burrows et al., 1986).

Denoting hyperons Λ, Σ and Ξ) by h, we define $x_{\sigma h} = \frac{g_{\sigma h}}{g_\sigma} = x_\sigma$, $x_{\omega h} = \frac{g_{\omega h}}{g_\omega} = x_\omega$, $x_{\rho h} = \frac{g_{\rho h}}{g_\rho}$, which are in the range from 1/3 to 1 (Glendenning et al., 1991). The parameter $x_{\rho h}$ is selected by quark SU(6) symmetry (Schaffner et al., 1996; Schaffner-Bielich et al., 2000). The calculation results show that the bigger $x_{\sigma h}$ and $x_{\omega h}$ are, the bigger PNS mass is (Zhao, 2019). Therefore, in order to obtain the largest possible mass of the PNS, we must choose the largest possible hyperon coupling parameters $x_{\sigma h}$ and $x_{\omega h}$. We select $x_{\omega h}$=0.9 and $x_{\sigma h}$ can be obtained by the following formula (Glendenning, 1997)

$$U_h^{(N)} = m_n \left(\frac{m_n^*}{m_n} - 1\right) x_{\sigma h} + \left(\frac{g_\omega}{m_\omega}\right)^2 \rho_0 x_{\omega h}, \tag{10}$$

where we choose hyperon-potentials as follows $U_\Lambda^{(N)} = -30$ MeV (Weissenborn et al, 2012; Gal et al., 2016), $U_\Sigma^{(N)}$=30 MeV (Schaffner-Bielich et al., 2000; Weissenborn et al, 2012; Gal et al., 2016; Batty et al., 1997) and $U_\Xi^{(N)} = -14$ MeV (Harada et al., 2010). We choose $x_{\sigma^* h}$ and $x_{\phi h}$ as follows (Schaffner et al., 1994)

$$x_{\sigma^*\Lambda} = x_{\sigma^*\Sigma} = 0.69, x_{\sigma^*\Xi} = 1.25, \tag{11}$$

$$x_{\phi\Lambda} = x_{\phi\Sigma} = -\frac{\sqrt{2}}{3}, x_{\phi\Xi} = -\frac{2\sqrt{2}}{3}. \tag{12}$$

Without considering the contributions from σ^* and ϕ mesons, we calculate the PNS by using the above eight groups of nucleon coupling parameters, and find that only the maximum masses (denoted as M_{max}) of the PNS obtained by DD-MEI, TW99 and GM1 are greater than that of the PNS PSR J0740+6620 (see Fig. 1). Among these three sets of parameters, the mass and

radius of the PNS PSR J0740+6620 given by GM1 are in agreement with the results of Fonseca et al. ($M = 2.08^{+0.07}_{-0.07}$ $M_\odot$ (Fonseca et al., 2021)) and Miller et al.(R=$13.7^{+2.6}_{-1.5}$ km (Miller et al., 2021)). Therefore, we use GM1 to study the influence of the contributions from σ^* and ϕ mesons on the surface gravitational redshift of the PNS PSR J0740+6620.

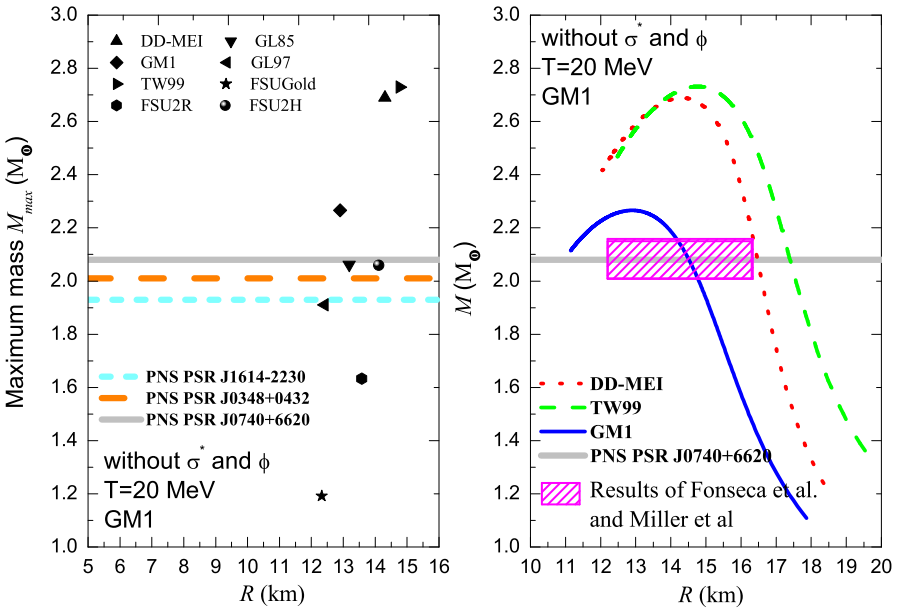

Figure 1. The relationship between the mass M or the maximum mass M_{max} of the PSR J0740+6620 and the radius R of the PNS. The contributions from σ^* and ϕ mesons are not considered in the calculation. The PNS's temperature is chosen as T=20 MeV.

4. The energy density and the pressure in the PNS PSR J0740+6620

The upper half of Fig. 2(a) shows the energy density ε of the PNS as a function of the pressure p. The lower half of Fig. 2(b) represents an enlarged view of the curve in the box in (a). The PNS's temperature is assumed to be 20 MeV. The red real curve does not consider the contributions from σ^* and ϕ mesons, while the green virtual curve does. The curve ends at the central energy density ε_c and the central pressure p_c of the PNS PSR J0740+6620.

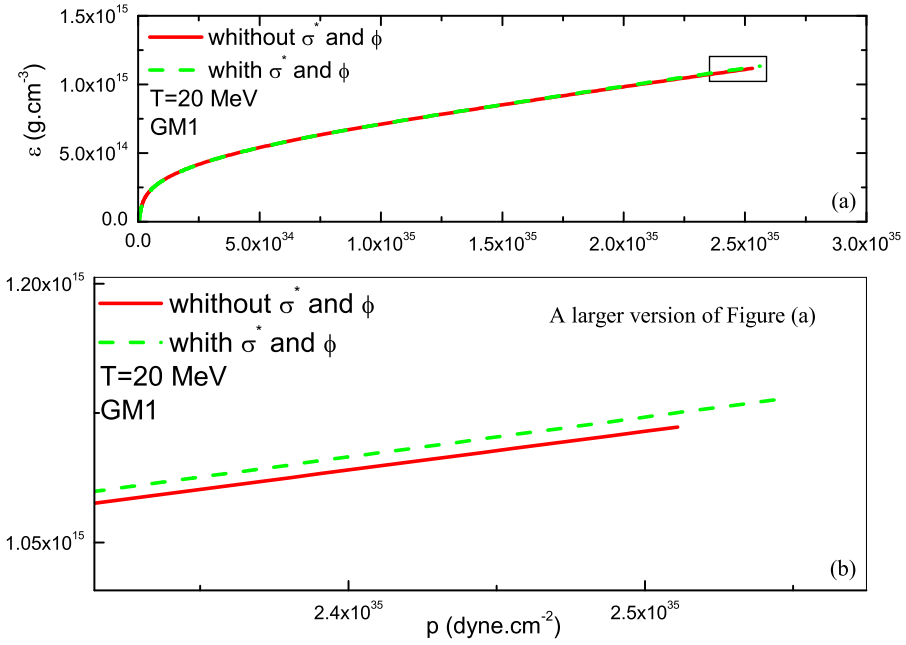

Figure 2. (a) The energy density ε of the PNS as a function of the pressure p. (b) A magnified view of the curve in the box in figure (a). The PNS's temperature is assumed to be 20 MeV. The red real curve does not consider the contributions from σ^* and ϕ mesons, while the green virtual curve does. The curve ends at the central energy density ε_c and the central pressure p_c of the PNS PSR J0740+6620.

We can see from Fig. 2(a) that the energy density ε of the PNS increases as the pressure p increases. We also see that the energy density ε increases relative to the same pressure p, taking into account the contributions from σ^* and ϕ mesons. Under the constraint of mass M=2.08 $M_\odot$, considering the contributions from σ^* and ϕ mesons, the central energy density of the PNS PSR J0740+6620 increases by about 0.89% from ε_c=1.013×10^{15} g.cm^{-3} to ε_c=1.022×10^{15} g.cm^{-3} (see Table 1); the central pressure of the PNS PSR J0740+6620 increased from p_c=2.118×10^{35} dyne.cm^{-2} to p_c=2.134×10^{35} dyne.cm^{-2}, increasing by about 0.76%.

5. The radius and the surface gravitational redshift of PNS PSR J0740+6620

The PNS's mass M and radius R as a function of the central energy density ε_c are shown in Fig. 3. The left ordinate represents the mass of the PNS, and

Table 1. The calculation results of PNS PSR J0740+6620 in this work. The mass of PNS PSR J0740+6620 is $M = 2.08$ $M_\odot$. ε_c, p_c, R, M/R and z are the central energy density, the central pressure, the radius, the mass radius ratio and the surface gravitational redshift of PNS PSR J0740+6620, respectively.

parameter	unit	without σ^* and ϕ	with σ^* and ϕ	percentage
ε_c	g.cm^{-3}	1.013×10^{15}	1.022×10^{15}	0.89%
p_c	dyne.cm^{-2}	2.118×10^{35}	2.134×10^{35}	0.76%
M/R	$M_\odot$/km	0.14327	0.14338	0.08%
R	km	14.518	14.507	-0.08%
z		0.31663	0.31718	0.17%

the right ordinate represents the radius of the PNS. The PNS's temperature is assumed to be 20 MeV. The red real curve does not consider the contributions from σ^* and ϕ mesons, while the green virtual curve does.

We see that the mass M of the PNS increases and the radius R decreases as the central energy density ε_c increases. Relative to the same central energy density, the mass of the PNS decreases and the radius increases, taking into account the contributions from σ^* and ϕ mesons. Under the constraint of mass M=2.08 $M_\odot$, considering the contributions from σ^* and ϕ mesons the radius of the PNS PSR J0740+6620 decreases by about -0.08% from R=14.518 km to R=14.507 km (see Table 1).

Figure 4 gives the mass radius ratio M/R and the surface gravitational redshift z of the PNS as a function of the central energy density ε_c. The PNS's temperature is assumed to be 20 MeV. The red real curve does not consider the contributions from σ^* and ϕ mesons, while the green virtual curve does. The curve ends at the central energy density ε_c and the central pressure p_c of the PNS PSR J0740+6620.

We see that the mass radius ratio M/R and the surface gravitational redshift z of the PNS all increase with the increase of the central energy density ε_c. Relative to the same central energy density ε_c, the mass radius ratio M/R and the surface gravitational redshift z of the PNS are reduced considering the contributions from σ^* and ϕ mesons. As it can also be seen from Fig. 4 and Table 1, under the limit of mass M=2.08 $M_\odot$, the mass radius ratio of PNS PSR J0470+6620 increases from M/R=0.14327 $M_\odot$/km to M/R=0.14338 by about 0.08%, and the surface gravitational redshift of PNS PSR J0470+6620 increases by about 0.17% from z=0.31663 to z=0.31718, taking into account the contributions from σ^* and ϕ mesons.

Fig. 5, Fig. 6 and Fig. 7 respectively show the variation of the surface gravitational redshift z of the PNS with the radius R, the mass M and the mass radius ratio M/R. Figure (b) in Figs. 5 and 6 are enlarged views of the curves in the boxes in corresponding figures (a), respectively. In Fig. 7, in order to sep-

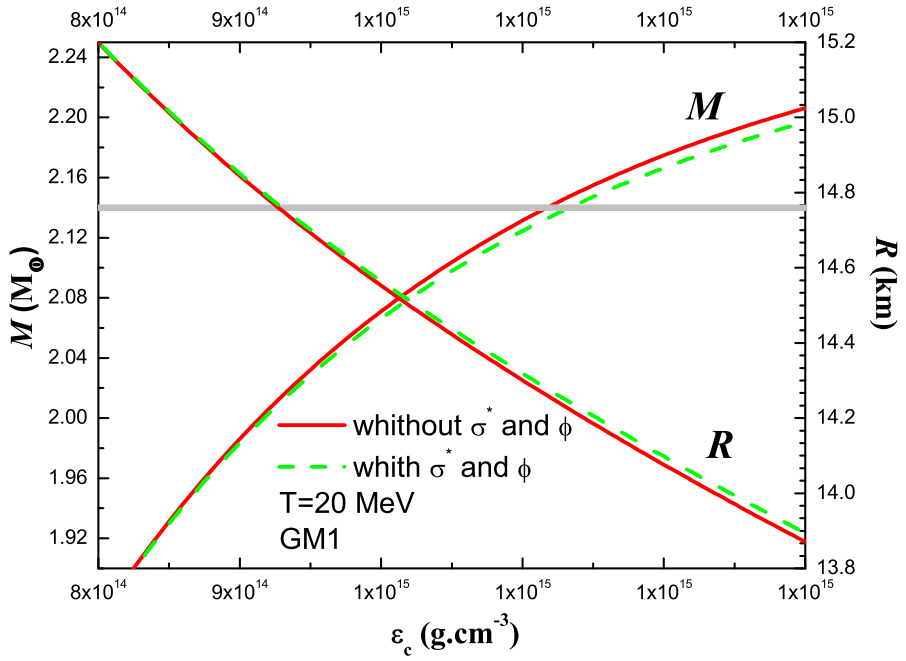

Figure 3. The PNS's mass M and radius R as a function of central energy density ε_c. The left ordinate represents the mass of the PNS, and the right ordinate represents the radius of the PNS. The PNS's temperature is assumed to be 20 MeV. The red real curve does not consider the contributions from σ^* and ϕ mesons, while the green virtual curve does.

arate the curves that take into account the contributions from σ^* and ϕ mesons and those that do not, we add 0.01 to the curve that takes into account the contributions from σ^* and ϕ mesons, that is, $z \to z + 0.01$.

Relative to the same radius R, the surface gravitational redshift z of the PNS decreases, taking into account the contributions from σ^* and ϕ mesons (see Fig. 5). Similarly, given the contributions from σ^* and ϕ mesons, the surface gravitational redshift z of the PNS increases relative to the same mass M (see Fig. 6). As it can also be seen from Fig. 7, considering the contributions from σ^* and ϕ mesons, the surface gravitational redshift of the PNS does not change with respect to the same mass radius ratio M/R, which can be known by formula (9).

In addition, under the constraint of mass M=2.08 $M_\odot$, the radius R of PNS PSR J0740+6620 will decrease, and the mass-radius ratio M/R and surface gravitational redshift z of PNS PSR J0740+6620 will increase (see Fig. 5, Fig. 6, Fig. 7 and Table 1).

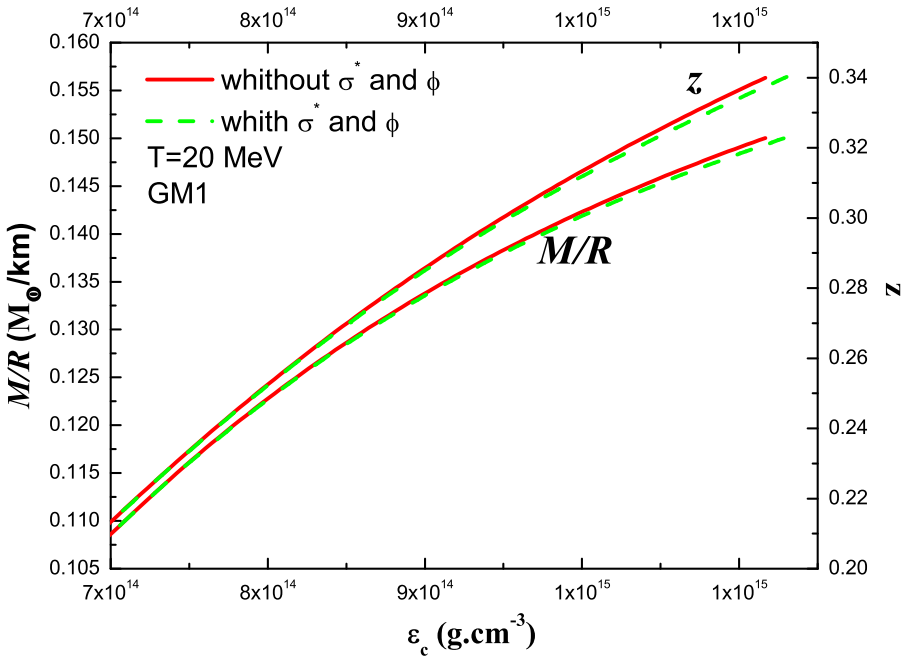

Figure 4. The mass radius ratio M/R and the surface gravitational redshift z of the PNS as a function of the central energy density ε_c. The PNS's temperature is assumed to be 20 MeV. The red real curve does not consider the contributions from σ^* and ϕ mesons, while the green virtual curve does. The curve ends at the central energy density ε_c and the central pressure p_c of the PNS PSR J0740+6620.

Given the mass of the PNS PSR J0740+6620 by Fonseca et al. (Fonseca et al., 2021), and the radius by Miller et al. (Miller et al., 2021), we can calculate the mass radius ratio to be 0.1233 $M_\odot$/km$<M/R<$0.1762 $M_\odot$/km and the surface gravitational redshift of the PNS PSR J0740+6620 to be $0.2541<z<0.4440$ (see the shaded boxes in Fig. 5-Fig. 7). It can be seen that our calculated results are in good agreement with the observed values.

The above results are valid for spherically symmetric static PNSs. For a rotating NS, the maximum mass increases by about 20%, and the NS becomes axisymmetric (Cook et al., 1994). The gravitational redshift of a rotating NS is a little more complicated than the previous NS as static and spherically symmetric, where we need to consider the polar redshift z_p, the equatorial redshift in the backward direction z_b, and the quatorial redshift in the forward direction z_f (Tu et al., 2022).

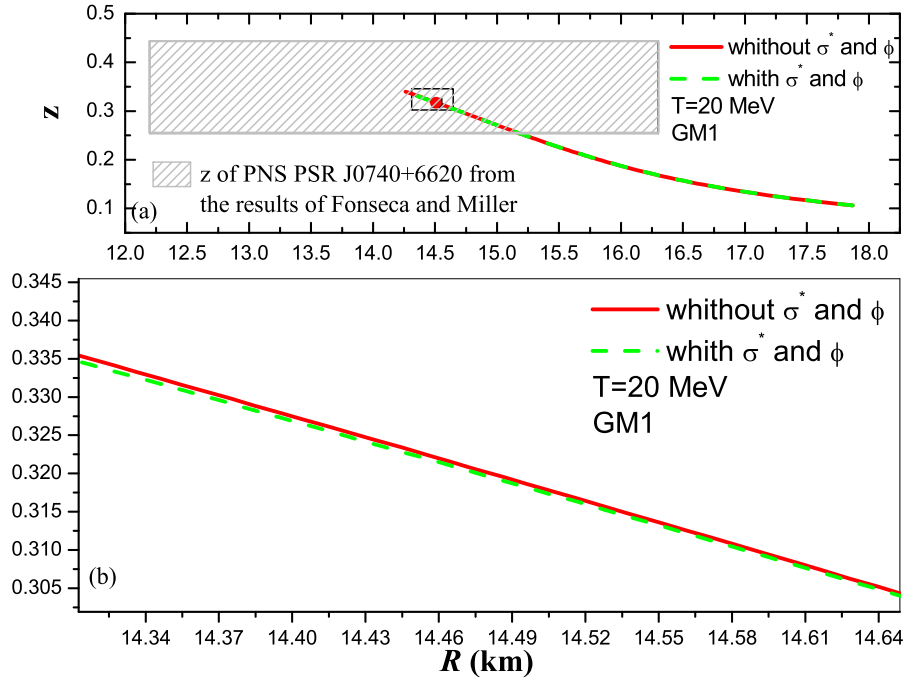

Figure 5. (a) The PNS's surface gravitational redshift z as a function of the radius R. (b) A magnified view of the curve in the box in figure (a). The PNS's temperature is assumed to be 20 MeV. The red real curve does not consider the contributions from σ^* and ϕ mesons, while the green virtual curve does. The curves end at the radius R of the PNS PSR J0740+6620.

6. Summary

We studied the effect of the contributions from σ^* and ϕ mesons on the surface gravitational redshift of PNS PSR J0740+6620 with RMF theory in consideration of a baryon octet. Here, we use eight sets of nucleon coupling constants GL85, GL97, GM1, DD-MEI, TW99, FSUGold, FSU2R and FSU2H to calculate the PNS. The temperature of the PNS is chosen as T=20 MeV. We find that only three of them (DD-MEI, GM1 and TW99) can give the PNS PSR J0740+6620's mass. We use GM1 to describe the PNS PSR J0740+6620.

The energy density ε of the PNS increases as the pressure p increases. The PNS's radius R decreases while the mass M, the mass-radius ratio M/R and the surface gravitational redshift of PNS increase with the increase of the central energy density ε_c.

The energy density ε increases relative to the same pressure p, taking into

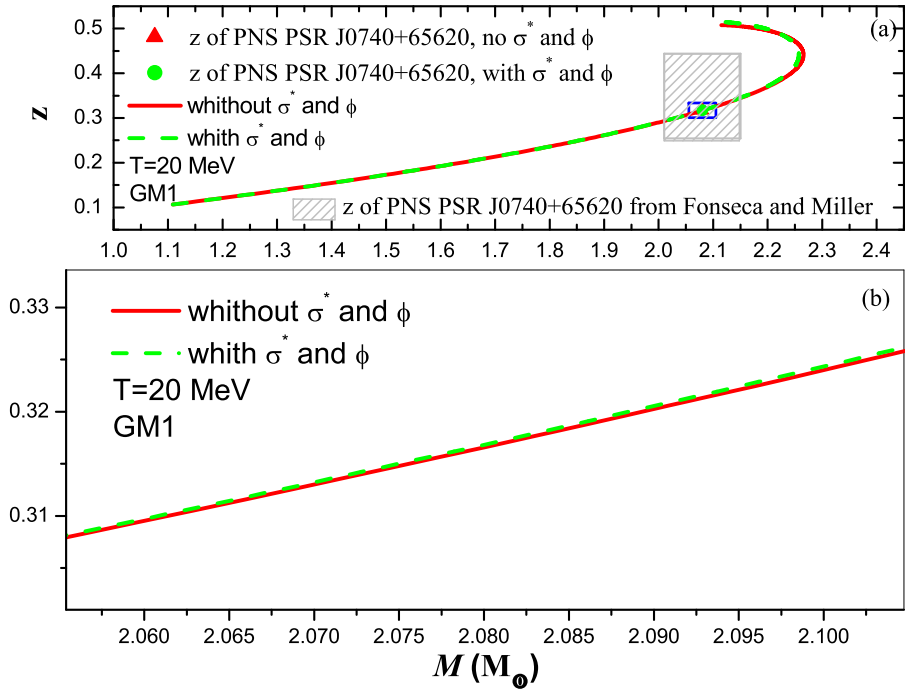

Figure 6. (a) The PNS's surface gravitational redshift z as a function of the mass M. (b) A magnified view of the curve in the box in figure (a). The PNS's temperature is assumed to be 20 MeV. The red real curve does not consider the contributions from σ^* and ϕ mesons, while the green virtual curve does.

account the contributions from σ^* and ϕ mesons. Relative to the same central energy density, the radius R of the PNS increases while the mass M, the mass-radius ratio M/R and the surface gravitational redshift z of the PNS decrease, taking into account the contributions from σ^* and ϕ mesons.

Under the constraint of mass M=2.08 $M_\odot$, considering the contributions from σ^* and ϕ mesons, for the PNS PSR J0740+6620, the radius decreases by about -0.08% from R=14.518 km to R=14.507 km, the central energy density increases by about 0.89% from ε_c=1.013×10^{15} g.cm^{-3} to ε_c=1.022×10^{15} g.cm^{-3}, the central pressure increased by about 0.76% from p_c=2.118×10^{35} dyne.cm^{-2} to p_c=2.134×10^{35} dyne.cm^{-2}, the mass radius ratio increases from M/R=0.14327 $M_\odot$/km to M/R=0.14338 by about 0.08%, and the surface gravitational redshift increases by about 0.17% from z=0.31663 to z=0.31718.

Taking into account the contributions from σ^* and ϕ mesons, the surface gravitational redshift z of the PNS decreases relative to the same radius R, and

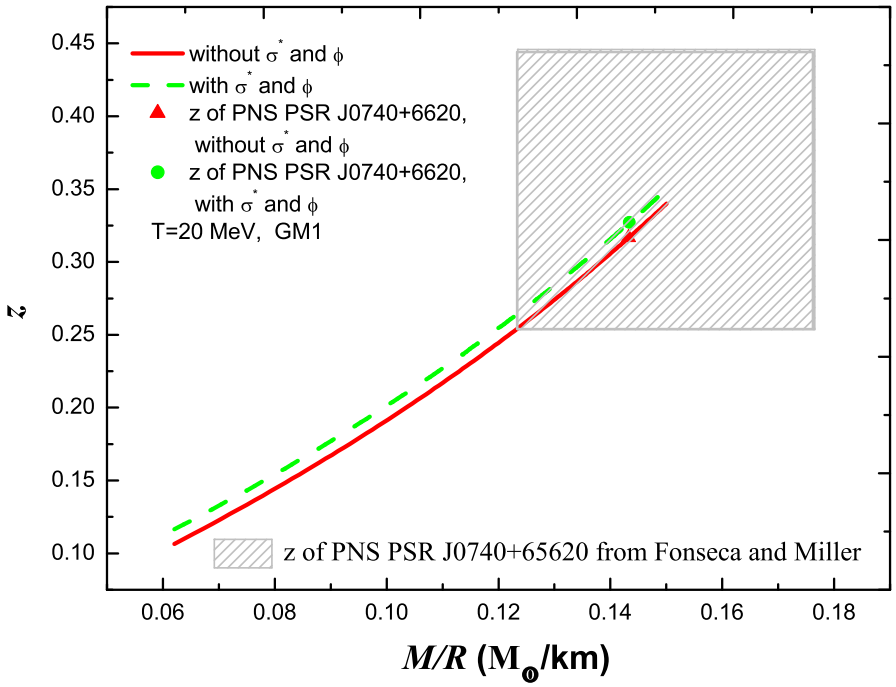

Figure 7. The PNS's surface gravitational redshift z as a function of the mass radius ratio M/R. The PNS's temperature is assumed to be 20 MeV. The red real curve does not consider the contributions from σ^* and ϕ mesons, while the green virtual curve does. The curves end at the mass radius ratio M/R of the PNS PSR J0740+6620. In order to separate the curves that take into account the contributions from σ^* and ϕ mesons and those that do not, we add 0.01 to the curve that takes into account the contributions from σ^* and ϕ mesons, that is, $z \to z + 0.01$.

increases relative to the same mass M, but does not change with respect to the same mass-radius ratio M/R

After accounting for the contributions of σ^* and ϕ mesons, the radius and surface gravitational redshifts are slightly changed compared to the case without σ^* and ϕ mesons. But the changes are too small to be inffered from astronomical observations.

Acknowledgements. This work was supported by the Natural Science Foundation of China (Grant No. 11447003).

References

Antoniadis J., Freire P.C.C., Wex N., et al. 2013, *Science*, 340, 448

Batty C.J., Friedman E., Gal A. 1997, *Phys. Rev.*, 287, 385

Burrows,A., Lattier,J.M. 1986, *Astrophys.*, **307**, 178

Cook,G.B., Shapiro,S.L., Teukolsky,S.A., 1994, *Astrophys.J.*, **424**, 823

Cromartie,H.T., Fonseca,E., Ransom,S.M., et al. 2020, *Nat.Astron.*, **4**, 72

Degollado, J.C., Salgado, M., Alcubierre, M.: 2020, *Phys. Lett.*, **B808**, 135666

Demorest,P.B., Pennucci,T., Ransom,S.M., et al. 2010, *Nature*, **467**, 1081

Ding, W.B., Cai, M.D., Chan A.H., Xu, Y.: 2022, *Int.J.Mod.Phys.*, **A37**, 2250034

Fonseca,E., Pennucci,T. T., Ellis,J.A., et al. 2016, *Astrophys. J.*, **832**, 167

Fonseca,E., Cromartie,H.T., Pennucci,T.T., et al. 2021, *Astrophys. J. Lett.*, **915**, L12

Gal,A., Hungerford,E.V., Millener,D.J. 2016, *Rev.Mod.Phys.*, **88**, 035004

Glendenning,N.K. 1985, *Astrophys. J.*, **293**, 470

Glendenning,N.K. 1987, *Phys.Lett.B*, **185**, 275

Glendenning,N.K. 1987, *Nucl.Phys.A*, **469**, 600

Glendenning,N.K. 1997, Compact Stars: Nuclear Physics, Particle Physics, and General Relativity (Springer-Verlag, New York, Inc)

Glendenning,N.K., Moszkowski,S.A. 1991, *Phys.Rev.Lett.*, **67**, 2414

Han, S., Prakash, M. 2020, *Astrophys.J.*, **899**, 164

Harada,T., Hirabayashi,Y., Umeya,A. 2010, *Phys.Lett.*, **B690**, 363

Laura,T., Mario,C., Angels,R. 2017, *Publ.Astron.Soc.Aust.*, **34**, e065

Li, Y.X., Chen, H.Y., Wen, D.H., Zhang, J. 2021, *Eur.Phys.J.*, **A57**, 31

Miller,M.C., Lamb,F.K., Dittmann,A.J., et al. 2021, *Astrophys. J. Lett.*, **918**, L28

Mu, X.L., Jia, H.Y., Zhou, Z., Wang, H.: 2017, *Astrophys.J.*, **846**, 140

Oppenheimer,J.R., Volkoff,G.M. 1939, *Phys.Rev.*, **55**, 374

Prakash,M., Bombaci,I., Prakash,M., et al. 1997, *Phys. Rep.*, **280**, 1

Schaffner,J., Dover,C.B., Gal,A., et al. 1994, *Ann.Phys.*, **235**, 35

Schaffner,J., Mishustin,I.N. 1996, *Phys.Rev.*, **C53**, 1416

Schaffner-Bielich,J., Gal,A. 2000, *Phys.Rev.*, **C62**, 034311

Todd-Rutel,B.G., Piekarewicz,J. 2005, *Phys.Rev.Lett.*, **95**, 122501

Tolman,R.C. 1939, *Phys.Rev.*, **55**, 364

Tu,Z.H., Zhou, S.G., 2022, *Astrophys.J.*, **925**, 16

Typel,S., Wolter,H.H. 1999, *Nucl.Phys.A*, **656**, 331

Weissenborn,S., Chatterjee,D., Schaffner-Bielich,J. 2012, *Nucl.Phys.A*, **881**, 62

Zhao,X.F. 2019, *Int.J.Theor.Phys.*, **58**, 1060
Zhou,S.G. 2016, *Phys.Scr.*, **91**, 063008
Zhou, Y., Chen, L.W.: 2019, *Astrophys.J.*, **886**, 52

PRÁCE ASTRONOMICKÉHO OBSERVATÓRIA
NA SKALNATOM PLESE
LII, číslo 2

Zostavovateľ:	RNDr. Richard Komžík, CSc.
Vedecký redaktor:	RNDr. Augustín Skopal, DrSc.
Vydal:	Astronomický ústav SAV, Tatranská Lomnica
IČO vydavateľa:	00 166 529
Periodicita:	3-krát ročne
ISSN (on-line verzia):	1336-0337
CODEN:	CAOPF8
Rok vydania:	2022
Počet strán:	72

Contributions of the Astronomical Observatory Skalnaté Pleso are processed using
LaTeX 2ε CAOSP DocumentClass file 3.09 ver. 2021.